DISCLAIMER

ORNL/TM-2024/3528

Process–Property–Performance Mapping of Additively Manufactured 316H Stainless Steel Components

Caleb Massey
Peeyush Nandwana
Holden Hyer
Selda Nayir
Geeta Kumari
Josh Kendall
Chase Joslin
David Collins
Tim Graening Seibert
Amy Godfrey
Andres Marquez Rossy
Amir Ziabari

September 2024

M2CR-22OR0403062

ORNL/TM-2024/3528

Advanced Materials and Manufacturing Technologies Program

PROCESS–PROPERTY–PERFORMANCE MAPPING OF ADDITIVELY MANUFACTURED 316H STAINLESS STEEL COMPONENTS

Caleb Massey
Peeyush Nandwana
Holden Hyer
Selda Nayir
Geeta Kumari
Josh Kendall
Chase Joslin
David Collins
Tim Graening Seibert
Amy Godfrey
Andres Marquez Rossy
Amir Ziabari

September 2024

M2CR-22OR0403062

Prepared by
OAK RIDGE NATIONAL LABORATORY
Oak Ridge, TN 37831
managed by
UT-BATTELLE LLC
for the
US DEPARTMENT OF ENERGY
under contract DE-AC05-00OR22725

CONTENTS

LIST OF FIGURES

LIST OF TABLES

ABBREVIATIONS

AM	additive manufacturing
AMMT	Advanced Materials and Manufacturing Technologies
ANL	Argonne National Laboratory
DED	directed energy deposition
DMSCNN	dynamic multilabel segmentation convolutional neural network
DoE	design of experiments
EBSD	electron backscatter diffraction
HIP	hot-isostatic pressing
HT	heat treatment
HV	Vickers hardness
J–R	J-integral vs. crack extension relationship
LANL	Los Alamos National Laboratory
LPBF	laser powder bed fusion
NIR	near-infrared
ORNL	Oak Ridge National Laboratory
PAC	Powder Alloy Corporation
SEM	scanning electron microscopy
SA	solution-annealing
SR	Stress relief
SS	stainless steel
SSJ	Subsize Specimen with unspecified thickness (Japan designation)
SSJ2	Subsize Specimen 2 mils thick (Japan designation)
TCR	Transformational Challenge Reactor
VED	volumetric energy density
XCT	x-ray computed tomography
XRD	x-ray diffraction

ACKNOWLEDGMENTS

This research was sponsored by the US Department of Energy Office of Nuclear Energy's Advanced Materials and Manufacturing Technologies program under contract DE-AC05-00OR22725 with UT-Battelle LLC. The authors thank David Hoelzer and Alex Plotkowski for their thoughtful review of this report before publication. Additional appreciation is given to Kevin Hanson, Ryan Dalton, and Cody Taylor for assistance with specimen heat treatments and sectioning. The authors would also like to acknowledge Ryan Duncan for the detailed machining efforts for this project. Finally, the authors acknowledge the hard work of the metallography team, including Jim Horenburg and Daniel Newberry.

EXECUTIVE SUMMARY

The Advanced Materials and Manufacturing Technologies Program is focused on accelerating the development of advanced materials and components fabricated via additive manufacturing, and is using laser powder bed fusion (LPBF) of 316H stainless steel as an initial case study. In the previous fiscal year, miniature high-throughput specimens were printed on multiple LPBF systems to provide initial processing windows to minimize porosity and limit epitaxial grain growth during prints.

This fiscal year, scaled builds were completed on three different LPBF systems at ORNL: a GE Concept Laser M2, a Renishaw AM400, and an EOS M290. Builds on the Concept Laser were conducted on multiple powder lots and processing parameter ranges to provide microstructure effects on time-independent and time-dependent mechanical properties. Builds on the Renishaw were produced using Oak Ridge National Laboratory (ORNL)-optimized printing parameters and Argonne National Laboratory (ANL)-optimized printing parameters to compare outcomes of parallel process optimization efforts at different national laboratories on the same LPBF system. Similarly, the build completed on the EOS M290 replicated the processing parameters of builds completed at Los Alamos National Laboratory (LANL). Optical microscopy and electron backscatter diffraction characterization was completed on all builds.

In addition to the general round robin characterization, this work-package generated time-independent data, including tensile and fracture toughness test data on scaled Concept Laser builds as a function of processing parameters and post-build heat treatment. This analysis is complimentary to work in parallel work packages aiming to establish heat treatment and processing effects on time-dependent properties. It was found that although the stress-relief heat treatment provides the highest strength at lower-temperatures, tensile strength begins to converge at higher temperatures regardless of heat treatment condition. In addition, the more rigorous solution annealing and hot-isostatic pressing post-build heat treatments result in higher fracture toughness than the stress-relieved condition.

The root-causes of the lower fracture toughness of the stress-relieved LPBF 316H material was informed via a stress-relief optimization study on a scaled concept laser print, where it was found that although dislocation recovery was largely complete after only a couple hours at 650°C, the extended hold of the current 24h heat treatment employed on scaled builds likely caused increased carbide volume fractions along the LPBF 316H grain boundaries, thereby deteriorating crack propagation resistance. This trend was seen to become more deleterious with additional increases of stress-relief temperature to 750°C or 850°C. These results have helped inform a new optimal stress-relief annealing condition for LPBF 316H for future campaign testing (650°C for 2h).

1. INTRODUCTION

As part of the Advanced Materials and Manufacturing Technologies (AMMT) program's mission to lead innovation in both materials and manufacturing technologies for nuclear energy applications, one of the key goals is to establish a rapid qualification framework for new materials to be deployed in advanced reactors. This is a grand challenge because to date, only six materials are approved for use in Section III, Division 5, of the American Society of Mechanical Engineers *Boiler and Pressure Vessel Code*, which oversees the realm of elevated-temperature nuclear structural materials. Additionally, current qualification approaches, even for a conventionally produced material, take at least a decade to fully implement. Therefore, rapid qualification of new additively manufactured materials is necessary to accelerate their nuclear application and enable advanced reactors to deploy in a more reasonable timeframe.

To demonstrate new approaches toward materials qualification, the AMMT program recently identified laser powder bed fusion (LPBF) as a uniquely challenging advanced manufacturing technology that, if implemented, could provide custom replacement parts and deploy complex valves, compact heat exchangers, and other geometrically complex components for both the existing nuclear fleet and various advanced reactor concepts. The challenges related to LPBF stem from variability in microstructure and material properties that can be a result of the powder feedstock [1], process parameters [2], geometry [3], or the additive manufacturing (AM) system used [4]. The intrinsic heterogeneity in LPBF components makes current code qualification initiatives impractical because fundamental assumptions regarding sampling material, grain structure, chemical distributions, and more are not translatable between wrought and additively manufactured components.

To explore qualification pathways for elevated temperature LPBF components, the AMMT program downselected 316H stainless steel (SS) as an initial material upon which to develop an accelerated code case strategy. The choice of LPBF 316H SS was a decision made from both a practical standpoint (because significant data repository on 316H wrought and weldment properties already exists) and a strategic one (because existing code cases are already under development within the American Society of Mechanical Engineers for LPBF and directed energy deposition (DED) 316L for lower-temperature operation). Therefore, the success of an elevated-temperature LPBF 316H SS code case would immediately benefit the nuclear industry and demonstrate rapid qualification techniques for use on other material and manufacturing technology combinations.

Before applying some of these accelerated techniques (e.g., machine learning–based algorithms to enable fewer high-temperature creep tests, multiscale modeling to extrapolate existing creep data, the use of viscoplastic models to consider anisotropic deformation of additively manufactured components), some degree of process optimization is necessary. This process optimization is used to (1) identify the most-relevant processing parameters influencing high-temperature performance and (2) provide an understanding about what an optimized LPBF 316H SS component design window looks like. This information is used to bound modeling and experiments for a relevant code case data package.

In FY 2023, a collaboration between three national laboratories, including Oak Ridge National Laboratory (ORNL), Argonne National Laboratory (ANL), and Los Alamos National Laboratory (LANL), began to develop a machine-agnostic methodology for LPBF 316H SS process optimization. Specifically, the three labs are printing various 316H SS powder compositions on three different AM units. Both ORNL and ANL have access to a Renishaw AM400, ORNL and LANL have access to an EOS M290, and ORNL is continuing to use the Concept Laser M2 unit that was heavily leveraged during the prior Transformational Challenge Reactor (TCR) campaign. The goal of this collaboration is to generate, through parallel optimization efforts, what can be considered as three unique heats of LPBF 316H SS that can be used for round-robin property comparisons and campaign testing.

Over the course of FY 2023, work at ORNL explored the sources of heterogeneity in LPBF 316H SS. In parallel, through innovative designs of experiments (DoEs) on both the Concept Laser M2 and Renishaw AM400 LPBF systems, researchers demonstrated that geometrically complex miniature specimens (called *Zeiss specimens* in prior work) could be combined with in situ monitoring and high-throughput x-ray computed tomography (XCT) to identify printing parameters that were >99.9% dense on the Concept Laser and >99.6% dense on the Renishaw AM400 [5].

This year (FY 2024), the scaling of these optimized printing parameters was demonstrated, and time-independent material properties have been collected at temperatures up to 600°°C for samples printed on the ORNL Concept Laser. As such, this report summarizes the effects of processing parameters and heat treatments on the performance of scaled LPBF 316H SS to inform future accelerated qualification efforts by the AMMT program. Scaled round-robin builds were also printed with preliminary microstructure information on EOS and Renishaw printers to compare with collaborating laboratories in future campaign testing. Additionally, the high-throughput XCT capability was expanded to compare porosity distributions in the small Zeiss specimens with subsized and full-size mechanical test specimens.

2. MATERIALS AND METHODS

2.1 FEEDSTOCK MATERIAL AND AVAILABLE AM UNITS

The chemistries of 316H SS powder feedstocks procured from Praxair Surface Technologies and Powder Alloy Corporation (PAC) are summarized in Table 1 and compared with the ASTM International's specifications. The powder feedstock chemistry ranges used for LPBF were based on compositions developed for conventionally processed material, such as ASTM A240 specification for rolled 316 SS plate material [6]. The powders had a nominal size distribution of 15–45 μm.

Of the different powders used across the three laboratories, the Praxair Lot 2 (0.06% C) powder was printed on both Renishaw AM400 units at ORNL and ANL. Similarly, Praxair Lot 4 powder (0.07% C) was printed on both the EOS M290 systems at LANL and ORNL. Finally, varied compositions were printed at all three national laboratories to provide varying heats for campaign testing.As illustrated in Figure 1, not all powders were printed on all units or at all collaborating institutions, but an overlap exists to ensure effective interlaboratory collaboration. As of the writing of this report, power/unit combinations in green have been printed, and those in black are possible to incorporate into the future work scope. For brevity, because ofthe characterization of specimens in this report are to powder and LPBF unit combinations identified in red in Figure 1.

Table 1. The ASTM specifications [6] for 316 SS and the measured feedstock powder chemistry for the powders used in this study. The compositions are in weight percent based on reported data from either material specifications from the vendor or chemical analysis reports from Dirats Laboratories.

Material		316H SS	316H SS	316H SS	316H SS	ASTM Specification
Vendor		Praxair	Praxair	PAC	Praxair	
Lot #		2	3	AMP316H1001E	4	
Composition (wt %)	Fe	balance	balance	balance	Balance	balance
	Cr	16.8	17.0	16.94	16.7	16.0–18.0
	Ni	12.1	12.3	10.88	11.9	10.0–14.0
	Mo	2.5	2.3	2.23	2.6	2.00–3.00
	Mn	1.13	1.05	1.02	0.02	<2.00
	Si	0.48	0.07	0.37	0.04	<1.00
	Al	0.01	0.02	0.01	0.01	n/a
	N	0.01	0.012	0.05	0.01	n/a
	O	0.034	0.03	0.048	0.02	n/a
	P	<0.005	<0.005	0.031	<0.005	<0.045
	S	0.00	0.00	0.00	0.00	<0.03
	C	0.06	0.08	0.043	0.07	<0.03 (L) 0.04–0.10 (H)

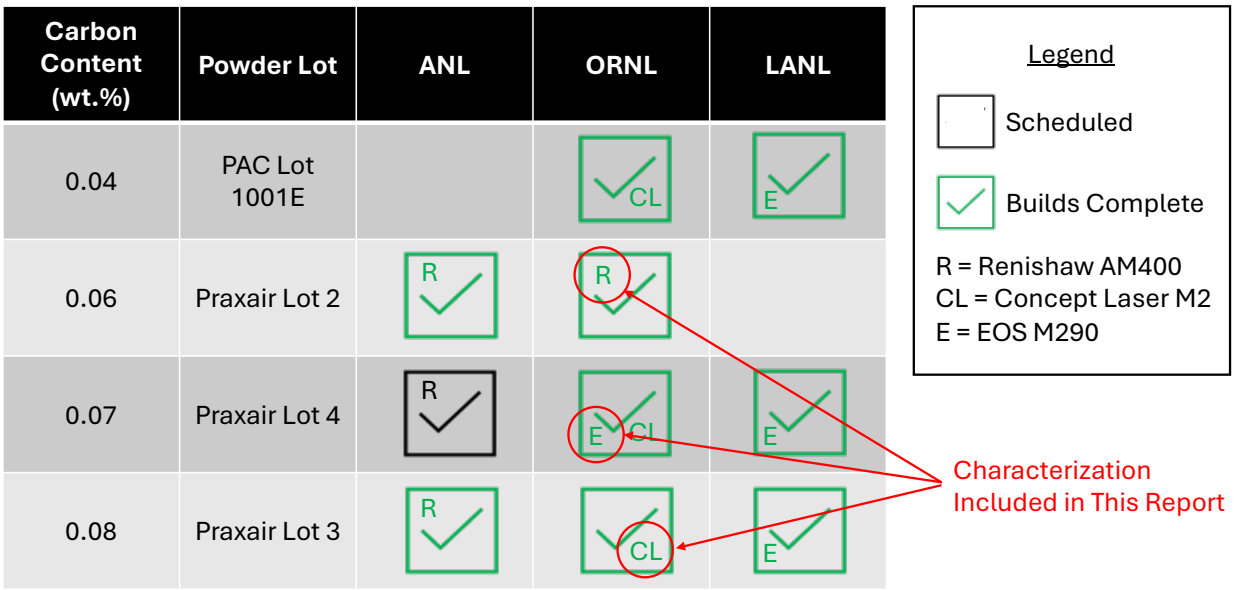

Figure 1. Schematic showing available and printed powder/machine combinations at each of the three national laboratories engaged in LPBF process optimization.

2.2 BUILDS COMPLETED IN FY 2024

2.2.1 Concept Laser Prints

Figure 2 shows PAC 0.04% C 316H SS DOE build made using the Concept Laser M2 on October 11, 12, and 16, 2023. These prints are repeats of DOEs 1, 3, and 4 from the FY 2023 report [5]. Similarly, sFigure 2 shows three tensile block builds printed in FY 2024 using Praxair/Linde Lot 4 0.07% C 316H SS. These prints are repeats of DOEs 1, 3, and 4 from the FY 2023 report and the same as PAC DOEs 1, 2, and 3 shown in Figure 2.

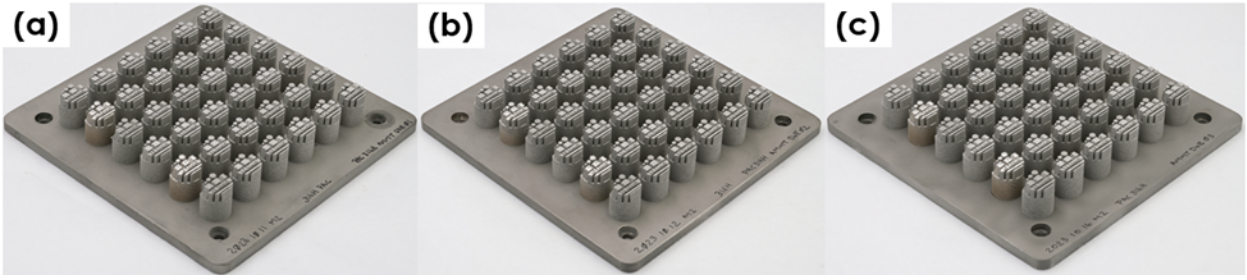

Figure 2. (a) 2023-10-11 PAC_316H_AMMT_DOE_01, (b) 2023-10-12 PAC_316H_AMMT_DOE_02, and (c) 2023-10-16 PAC_316H_AMMT_DOE_03.

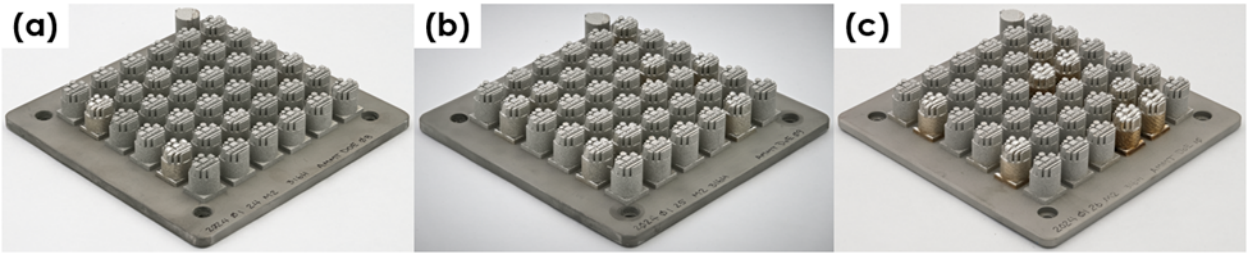

Figure 3. (a) 2024-01-24 M2_AMMT_DOE_08, (b) 2024-01-25 M2_AMMT_DOE_09, and (c) 2024-01-26 M2_AMMT_DOE_10.

Figure 4 shows three tensile block builds printed in FY 2024 using Praxair/Linde Lot 3 0.08% C 316H SS. These builds were printed with volumetric energy densities (VEDs) of 71, 52, and 135 J/mm^3 for Tensile Blocks 01 Repeat, Tensile Blocks 02 Repeat, and Tensile Blocks 04, respectively, and had print times of approximately 91, 55, and 92 h, respectively. The additional tensile bar shown in 2024-01-12 M2 AMMT Tensile Blocks 04 was printed for data capture purposes with Laser Module 2 and did not affect the print time. The 2024-01-12 M2 AMMT Tensile Blocks 04 sample had a build pause at layer 2033, or 101.75 mm in height, because of a loss of building air pressure. The typical layer time was 246 s for this print, and the pause exceeded 2 days and 5 h. Nonetheless, this is well beyond the gauge region of these tensile bars and is considered negligible from effects on mechanical properties.Table 2 presents comprehensive processing parameters for all Concept Laser builds.

Figure 5 shows 2024-05-16 M2 316H Tensile Blocks 05, which used Praxair/Linde Lot 4 0.07% C 316H SS. This sample is the same as Tensile Blocks 01 and Tensile Blocks 01 Repeat with an added tensile bar at the back right of the start plate. As with 2024-01-12 M2 AMMT Tensile Blocks 04, this bar was printed for data capture purposes with Laser Module 2 and did not affect the print time of 92 h.

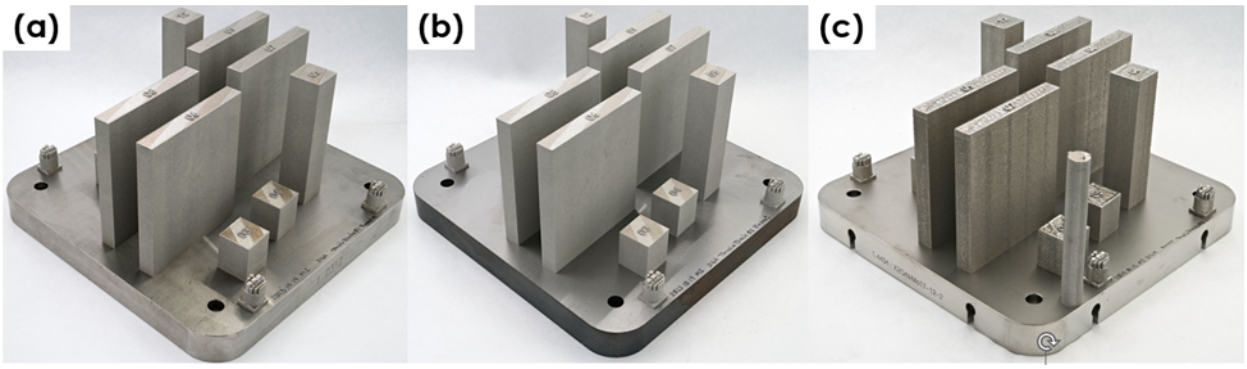

Figure 4. (a) 2023-10-19 M2 316H Tensile Blocks 01 Repeat, (b) 2023-10-24 M2 316H Tensile Blocks 02 Repeat, and (c) 2024-01-12 M2 AMMT Tensile Blocks 04.

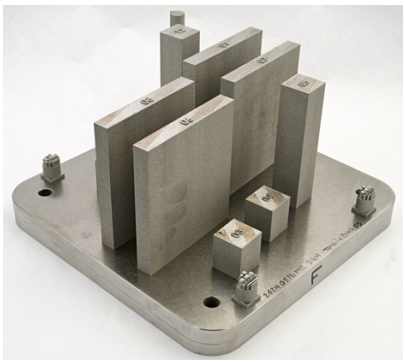

Figure 5. 2024-05-16 M2 316H Tensile Blocks 05, which is identical to the parameters printed for Tensile Blocks 01 and Tensile Blocks 01 Repeat with an added tensile bar at the back right of the start plate.

Table 2. Processing parameters of scaled AMMT Concept Laser builds. Constant stripe width (10 mm), stripe overlap (20 µm), and layer rotation (67°) for all processed samples. The powder compositions were represented with added C (wt %) and Cr_{eq}/ Ni_{eq} numbers.

Build	Power (W)	Scan velocity (mm/s)	Hatch spacing (µm)	Spot size (µm)	Layer thickness (µm)	VED (J/mm^3)	C (wt %)	Cr_{eq}/Ni_{eq}	Powder
Tensile Blocks 01	200	750	75	125	50	71.1	0.080	1.261	Praxair FE-455-N30 Lot 3
Tensile Blocks 02	290	1,500	75	130	50	51.6	0.080	1.261	Praxair FE-455-N30 Lot 3
Tensile Blocks 03	200	750	125	125	50	42.7	0.080	1.261	Praxair FE-455-N30 Lot 3
Tensile Blocks 01 (Repeat)	200	750	75	125	50	71.1	0.080	1.261	Praxair FE-455-N30 Lot 3
Tensile Blocks 02 (Repeat)	290	1,500	75	130	50	51.6	0.080	1.261	Praxair FE-455-N30 Lot 3
Tensile Blocks 04	380	750	75	125	50	135.1	0.080	1.261	Praxair FE-455-N30 Lot 3
Tensile Blocks 05	200	750	75	125	50	71.1	0.070	1.326	Praxair FE-455-N30 Lot 4

2.2.2 EOS Round Robin Print

Figure 6 shows three builds of AMMT DOE 01 printed on an EOS M290, designed samples to maintain as many similarities between machines as possible. Inherent differences from the printers include gas flow direction, which is parallel to the recoating direction on the Concept Laser M2 and perpendicular to the recoating direction on the EOS M290. Furthermore, the user cannot change the spot size on the EOS M290, which is calibrated by the manufacturer at around 90 µm. The EOS M290 has a heated build

platform option, but was not used because ORNL's Concept Laser M2 does not have a heated build platform. The first print in Figure 6(a) is 2024-06-28 EOS SI4325 AMMT DOE 01 failed because it exceeded the maximum allowed temperature, which was targeted at room temperature. The build exceeded a set point during printing for too long, which caused the machine to error out. The second print shown in Figure 6(b) is 2024-07-02 EOS SI4325 AMMT DOE 01 Repeat, which unfortunately had two parameters assigned incorrectly. This issue was fixed on Figure 6(c), which shows the third print, 2024-07-03 EOS SI4325 AMMT DOE 01 Corrected.

Figure 7 shows a repeat print from LANL, which printed roughly 4 in. block sections. This print took 192.5 h and was paused for approximately 70 s at layer 25.920 mm and approximately 100 s at layer 63.250 mm to lower the powder collector and prevent overflowing. All EOS print parameters are detailed in Table 3.

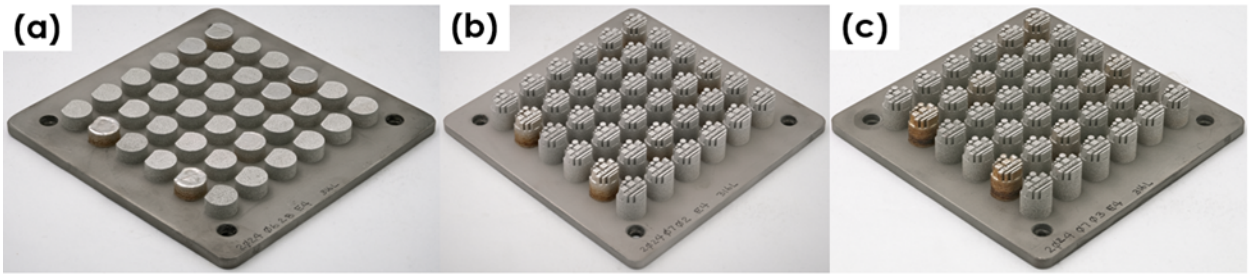

Figure 6. (a) 2024-06-28 EOS SI4325 AMMT DOE 01, (b) 2024-07-02 EOS SI4325 AMMT DOE 01 Repeat, and (c) and 2024-07-03 EOS SI4325 AMMT DOE 01 Corrected.

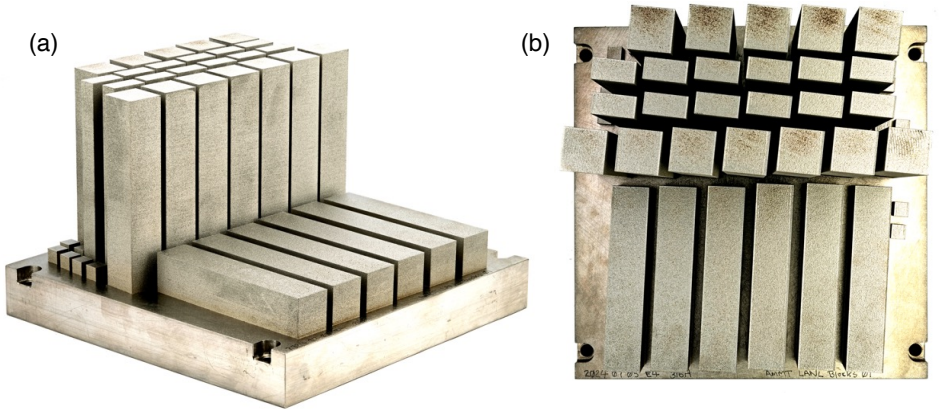

Figure 7. Round-robin EOS build (2024-07-05 EOS SI4325 AMMT LANL Blocks 01) for comparison with LANL, showing (a) isometric and (b) top views.

Table 3. Processing parameters of scaled AMMT EOS Build. Constants were stripe width (12 mm), stripe overlap (90 µm), and stripe angle (47°) for all processed samples. The powder compositions were represented with added C (wt %) and Cr_{eq}/ Ni_{eq} numbers. The color-coded print parameters legend is shown in Figure 8.

Color	Power (W)	Scan velocity (mm/s)	Hatch spacing (µm)	Approx. spot size (µm)	Layer Thickness (µm)	VED (J/mm^3)	C (wt %)	Cr_{eq}/Ni_{eq}	Powder
Red	275	688	0.14	0.09	0.04	71.4	0.070	1.326	Praxair FE-455-N30 Lot 4
Orange	240	600	0.14	0.09	0.04	71.4	0.070	1.326	Praxair FE-455-N30 Lot 4
Yellow	214	535	0.14	0.09	0.04	71.4	0.070	1.326	Praxair FE-455-N30 Lot 4
Green	257	644	0.14	0.09	0.04	71.4	0.070	1.326	Praxair FE-455-N30 Lot 4
Blue	227	567	0.14	0.09	0.04	71.4	0.070	1.326	Praxair FE-455-N30 Lot 4
Magenta	200	521	0.14	0.09	0.04	68.5	0.070	1.326	Praxair FE-455-N30 Lot 4

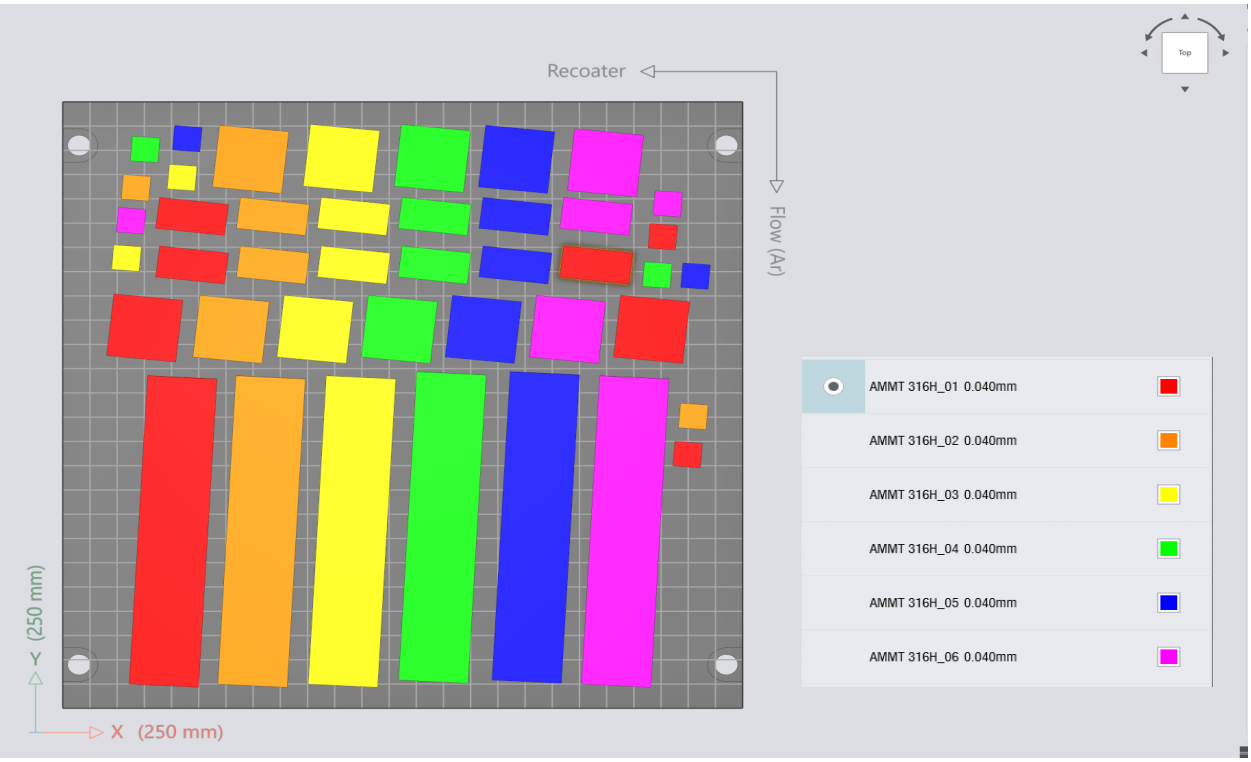

Figure 8. Round-robin EOS build layout with parameter color legend.

2.2.3 Renishaw Scaled ORNL and Round-Robin Prints

ANL's process mapping affirmed that the Renishaw recommended parameters for 316L SS were the best for processing the 316H-2 SS powder, which had an energy density of 53.2 J/mm^3, as described in Table 4. Plates that were 4 in. long and 12 mm thick were fabricated at ANL using the optimized parameters on the Renishaw AM400. Similar plates were fabricated on the Renishaw AM400 at ORNL using the ANL-optimized parameters (Figure 9(a).) However, ORNL determined that a slightly higher energy density (76.2 J/mm^3) was required to fabricate dense 316H SS for multiple different geometry types with. Therefore, 4 in. plates were also fabricated from the 316H-2 SS powder using the ORNL optimized parameter (Figure 9(b).)

Table 4. Process parameters optimized by ANL and ORNL for 316H SS

Parameter	Laser power (W)	Point distance (μm)	Dwell time (μs)	Hatch spacing (mm)	Layer thickness (mm)	Scan rotation (°)	Scan speed (mm/s)	Energy density (J/mm^3)
ANL Best	195	60	80	0.11	0.05	67	666.7	53.2
ORNL Best	200	70	110	0.09	0.05	67	583.3	76.2

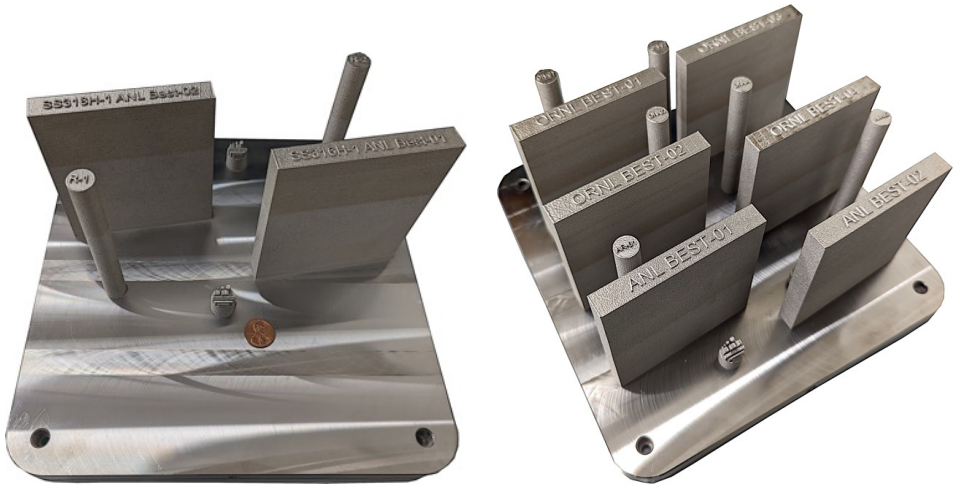

(a) SS316H-1 (b) SS316H-2

Figure 9. Round-robin Renishaw builds for comparison with ANL Renishaw Data, showing representative builds using recommended ANL and ORNL parameters.

2.3 CHARACTERIZATION METHODS

2.3.1 In Situ Data Analysis

Peregrine is an ORNL-developed software tool designed to provide a comprehensive suite of data collection, analysis, and visualization capabilities for powder bed AM systems. Peregrine is responsible for collecting and analyzing layer-wise imaging data for the LPBF printers used under the AMMT program. In support of various AMMT work packages, a common sensor package for in situ monitoring data was installed on three ORNL LPBF machines: the Concept Laser M2, the Renishaw AM250, and the Renishaw AM400. These sensors include a combination of high-resolution, visible-light images and temporally integrated, near-infrared (NIR) images. The data generated by these sensors have been integrated into the Peregrine software tool to support ex situ characterization efforts.

Each of these machines was instrumented with two cameras: a 20 megapixel visible-light camera (Basler acA5472-17um) and a 4.2 megapixel NIR-sensitive camera (Pixelink PL-D734MU-NIR-T). The visible-light camera was outfitted with an ultraviolet/NIR cutoff filter to protect the camera detector from the laser. Similarly, the NIR-sensitive camera had a narrow band-pass filter centered in the NIR range (808 ± 10 nm) as well as neutral density filters (outer diameter ≈ 1.8) to prevent image saturation. The visible light captured a post-melt and a post-recoat image for each layer, and the NIR camera produced a video buffer that was dynamically analyzed at the end of a layer, producing three images engineered to extract relevant process dynamics for the layer.

Data collected by each of the sensors described here was used to train a dynamic multilabel segmentation convolutional neural network (DMSCNN), which is the deep learning model that forms the backbone of

Peregrine's analysis capabilities. A trained DMSCNN may be used to detect various anomaly classes observable from the multimodal sensor signature of a given layer. Common anomaly classes include successfully printed material, unmelted powder, spatter particles, recoater events, powder short feeding, sensor anomalies, and more. Analysis of the anomaly segmentation results may be used to improve understanding of anomalous behavior with the LPBF process.

2.3.2 X-ray Computed Tomography Data Analysis

This FY, improvements to ORNL's XCT capabilities enabled high-throughput characterization of additional sample types in addition to the FY23 Zeiss specimen scans. XCT experiments were conducted using ZEISS's METROTOM 800 system with a procedure specifically designed for high-throughput characterization of full-sized creep, fatigue, and Subsize Specimen 2 (Japan designation; SSJ2) samples. for which custom holders were developed to facilitate the simultaneous scanning of multiple samples, enhancing efficiency and maintaining data quality.

Figure 10. Holders for various tensile specimens along with an example of a visualization of the simultaneous XCT of multiple SSJ2 coupons and detected/segmented flaws.

For creep and fatigue samples, each holder was designed to accommodate three samples simultaneously to optimize the scanning process. In contrast, the Subsize Specimen (Japan designation; SSJ) holders (capable of holding 0.5 and 0.75 mm thick samples) were capable of simultaneously scanning up to 40 samples. For clarity and separation during scanning, this work limited the load to eight samples per scan. Two of the holders were loaded on top of each other and scanned back-to-back, saving a time and labor.

To ensure precise imaging of the gauge sections of each creep or fatigue sample, this study performed two scans per sample—one focused on the top section and another on the bottom. These scans were subsequently stitched together to generate a complete image of the gauge section. To achieve high-throughput characterization, this study integrated deep learning models—notably, the Simurgh

algorithm—to significantly reduce scan times without compromising data quality. Traditionally, a single creep sample would require over an hour of scanning to obtain high-quality data. However, by scanning three samples simultaneously, this study reduced the scan time to approximately 20 min per half-gage section (40 min total per three samples).

For the CREEP samples, the scan was performed with 290 views and a 4 s integration time per view using a 220 kV source and a beam hardening filter to mitigate artifacts. The resulting voxel size was approximately 16 μm, allowing for the detection of defects larger than 15 μm. In contrast, the SSJ2 samples were scanned using a step-and-shoot method with 580 views at a 1 s integration time per view. This approach yielded a total scan time of 1,160 s for the full gage sections of eight samples. The voxel size for these scans was 8 μm with an expected detection capability for defects above 25 μm.

By leveraging these optimized scanning procedures along with advanced deep learning techniques, including Simurgh (to perform XCT reconstruction) and the 2.5D Deep Learning U-Net Model (for segmentation), this study successfully enhanced the throughput of XCT characterization for both creep and SSJ2 samples, allowing for an accelerated scanning process and accurate detection of critical defects. The following results sections summarize the results obtained for various mechanical testing and tensile geometries (SSJ2, creep, fatigue) and compare those results with component-level values, distinguishing the effect of geometry and process parameters on the flaw density in these samples.

2.3.3 Post Build Heat Treatments and Machining

Following printing, each part was sectioned from the baseplate and subjected to one of three heat treatments (HTs) prior to machining for high-temperature mechanical testing. The three HTs are shown in Table 5 and were selected to study the unique evolution of the microstructure when subjected to stress relief (SR), solution annealing (SA), or hot-isostatic pressing (HIP).

Table 5. HT parameters

HT	Type of HT	HT parameters
HT1	SR	650°C, 24 h, air-cooled
HT2	SA	1,100°C, 1 h, water-quenched
HT3	HIP	1,150°C, 100 MPa, 4 h

Following each respective HT, one of three varied machining methodologies was used depending on the research thrust, as illustrated in Figure 11. Generally, each large build contained four larger plates, three of which were subjected to one of each of the varied HTs. For elevated temperature creep and creep-fatigue testing, the plates were sent out for machining to external vendors with care taken to number the specimens sequentially to link to generalized locations harvested from the printed plate. The size of the plates allowed for three creep or fatigue conditions to be collected from one build plate/HT condition. Because of the existence of another parallel report on this topic, the precharacterization of select creep and creep-fatigue specimens is included in this work, but the time-dependent properties are summarized in a separate report [7].Following each respective heat treatment, one of three machining methodologies was used depending on the research thrust (Figure 11). Generally, each large build contained four larger plates, and three of which were subjected to one of each of the heat treatments. Pre-characterization of select creep and creep-fatigue specimens is included in this work, but time-dependent properties are summarized in a separate parallel report [7].

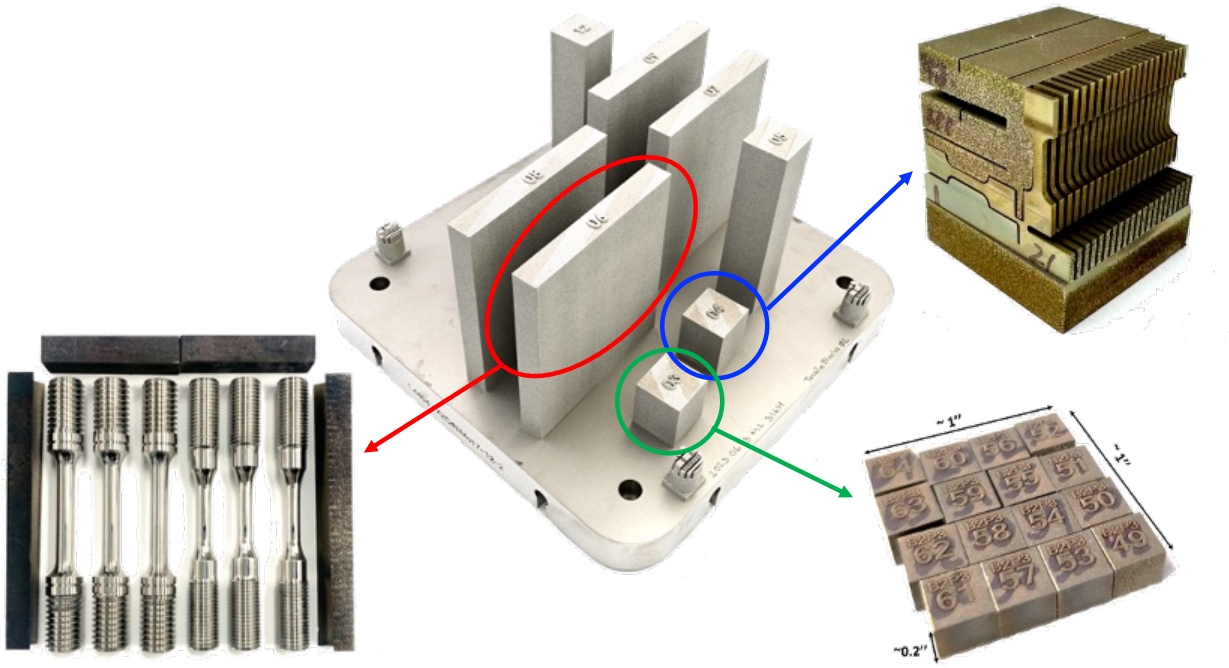

Figure 11. Machining schematic for heat treated blocks analyzed in this work. Machined specimens include full-sized creep and creep-fatigue specimens (red), miniature tensile/fracture toughness specimens (blue), and a representative layer of EDM'd cubes for stress-relief optimization (green).

In addition to the full-sized specimens, in-house wire electrical discharge machining was performed to machine either subsized tensile (SSJ2 geometry, 0.5 mm thick) or fracture toughness (MBS-1) specimens from heat-treated parts. From each 1 in. cube on the larger builds, 20 transverse- and 20 build-oriented SSJ specimens were able to be machined across the specimen thickness, as shown by the blue arrow image in Figure 11. Similarly, up to 12 fracture toughness specimens could be machined from each cube, providing specimens oriented such that crack propagation would occur in the build direction. General dimensions of the subsized tensile and fracture toughness specimens are provided in Figure 12.

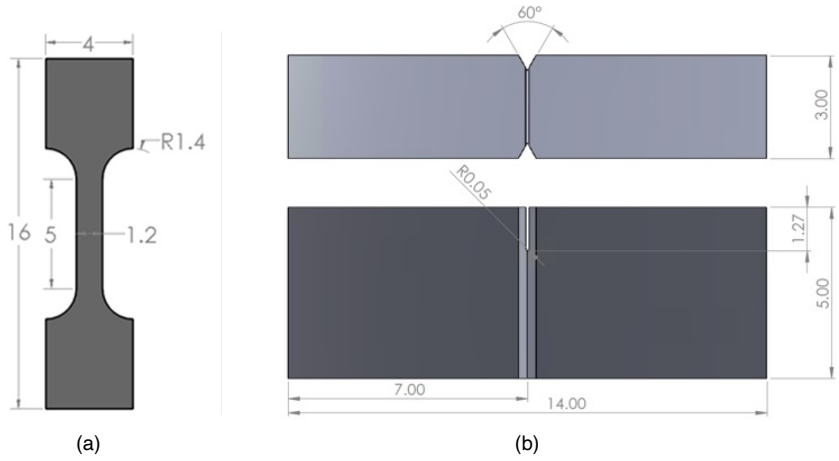

Figure 12. Nominal dimensions of (a) SSJ2 tensile geometry (0.5 mm thick) and (b) MBS-1 fracture toughness geometry. All measurements are in millimeters. In a separate research initiative, a select cube from build Tensile Blocks 02 (equivalent VED of approximately 52 J/mm^3) was used for an SR optimization study. This cube was systematically sectioned into smaller cubes using wire EDM, each section measuring approximately 0.25 × 0.25 × 0.2 in., as shown in Figure 11. In total, 80 smaller cubes were fabricated.

For the SR optimization study, the sectioned cubes of as-printed samples were heat-treated within a temperature range of 650°C–850°C and followed by air-cooling, as illustrated in the schematic diagram in Figure 13. Multiple cubes were heated at specific temperatures (e.g., 850°C) for varying durations, as detailed in Table 6. A single cube was extracted at each time point, ranging from 15 min to 6 h, to study the microstructural evolutions and the corresponding hardness and recovery. The HT at 650°C was extended to 24 h to further investigate the effects of prolonged exposure. All HTs were conducted in an open-air environment with a heating rate of 10°C/min using a box furnace.

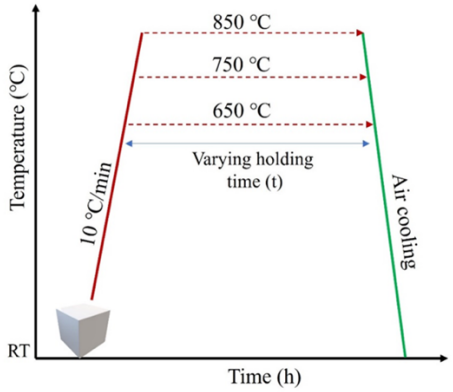

Figure 13. Schematic of scheduled HT for SR temperature optimization. Specimens were held at a temperature within a box furnace for specified times prior to air-cooling. Table 6. SR optimization HT parameters

Temperature	Time intervals							
850°C	15 min	30 min	1 h	2 h	3 h	4 h	5 h	6 h
750°C	15 min	30 min	1 h	2 h	3 h	4 h	5 h	6 h
650°C	15 min	30 min	1 h	2 h	3 h	4 h	5 h	6 h

2.3.4 Microstructure Characterization

For the SR optimization effort, both x-ray diffraction (XRD) and scanning electron microscopy (SEM) were used for microstructure characterization. Heat-treated samples were metallographically prepared for microstructural evaluation. Oxide layers formed during the HT were removed from all sides of the cube samples through a series of polishing steps. Mechanical polishing was performed using SiC abrasive papers with grit sizes of 400, 600, 800, and 1,200. Then, the polished samples were used for XRD analysis to quantify the recovery of the samples at each temperature and time. XRD data were acquired using a Rigaku SmartLab XRD system equipped with a Cu source in Bragg–Brentano reflection geometry. Data collection occurred within a 2θ range of 20°–120°, using a step size of 0.001° and a scan speed of 0.6°/min. The modified Williamson–Hall equation was used to measure the dislocation density:

$$\Delta K \cong \frac{0.9}{D} + \left(\frac{\pi M^2 b^2}{2}\right)^{\frac{1}{2}} \rho^{\frac{1}{2}} K C^{\frac{1}{2}} + O(K^2 C). \quad (1)$$

In this context, the parameter K is equal to $2\sin\theta/\lambda$, with ΔK representing the full width at half maximum. The variable D represents the average crystallite size, and $M = 2$ is a constant associated with the dislocation cutoff radius. The Burgers vector of ferrite, denoted by b, is 0.248 nm, and ρ is the average

dislocation density. The variable *C* signifies the average contrast factor of dislocations, and *O* refers to noninterpreted higher-order terms.

Following the XRD analysis, an oxalic acid electrolytic etching method was employed to reveal cell structures, grain boundaries, and other phases, which is a standard practice to rapidly screen austenitic SSs for the susceptibility to intergranular cracking. Electrolytic etching of samples was done on a solution prepared with 10 g of oxalic acid dissolved in 100 mL of distilled water and operated at 2.0 V under direct current. The 316L SS samples were etched for 90 s to reveal the fish-scale structure, and 316H SS samples were only etched for 20–50 s because of quickly darkened surfaces resulting from longer etching.

For SEM analysis (both SR optimization and general microstructure characterization), a Tescan MIRA3 GMH field emission SEM also equipped with an Oxford electron backscatter diffraction (EBSD) detector was used to collect grain size, texture, and morphology information for each build. Maps were collected using an accelerating voltage of 20 kV at step sizes ranging from 0.5 to 2 μm depending on the field of view analyzed. For large field-of-view grain mapping for texture and grain size analysis, a total field of at least 1 × 1 mm was surveyed. A grain structure and orientation were postprocessed using either the Aztec Crystal software, called EDAX OIM v8.1.0, or the MTEX MATLAB toolbox. The size of the cell structures and the volume fraction of the carbide phase were quantified using ImageJ software. Vickers microhardness measurements were conducted at room temperature on each sample using a Leco AMH 55-LM110 series tester equipped with a four-sided diamond pyramidal indenter. An average hardness value was calculated from 15 measurements per sample with a load of 500 gram-force applied for 15 s.

To assess potential heterogeneity along the build height of scaled parts, stress-relieved samples were characterized using a Zeiss Crossbeam 550 field emission SEM with Oxford detectors for EBSD imaging. The voltage was kept at 25 kV, the current was 20 nA, and the working distance was 14–17 mm. The exposure time ranged between 2 and 6 μs, and the total zero solution of the maps was between 0.3% and 8%. The total area of approximately 460 × 350 μm^2 was scanned using a 0.5 μm step size with 250× magnification and image dimensions of 1,024 × 768 pixels. Post-processing completed using the MTEX 5.8.2 MATLAB 2022b toolbox. Grains with more than 4° misorientation and 20 pixels were constructed as individual grains.

2.3.5 Mechanical Testing

SSJ2 specimens were tested in the shoulder-loading configuration under ambient conditions on a single-column Instron servomechanical test frame at a nominal strain rate of 0.015 mm/mm/min for room-temperature measurements or at a nominal strain rate of 0.005 mm/mm/min for elevated-temperature measurements. Time, crosshead displacement, load, and gauge cross section dimensions were recorded. Because strain was not measured directly and was computed based on crosshead displacement, a compliance correction method was employed so the approximate plastic strain values could be extracted from the crosshead displacement data:

$$\varepsilon_{\mathrm{p}} = \frac{\delta - P \times C_{\mathrm{LL}}}{l}, \tag{2}$$

where ε_{p} is the plastic strain; δ and *P* are the crosshead displacement and load, respectively; C_{LL} is the load line compliance calculated as the inverse of the elastic slope of the raw load–displacement curve; and *l* is the gauge length. When the load–displacement curve is converted to a stress–plastic strain curve, the pertinent tensile values can be calculated. The 0.2% offset yield strength is the stress at 0.2% plastic strain, the ultimate tensile strength is the maximum stress, the uniform elongation is the plastic strain

value corresponding to the ultimate tensile strength, and the total elongation is the plastic elongation at failure.

In addition to tensile testing, J-integral vs. crack extension relationship (J–R) fracture testing of MBS-1 specimens was also performed. Fatigue precracking and monotonic fracture testing were carried out on a dual-frame mechanical test system consisting of TestResources 810LE5 and 800LE3 frames. Precracking consisted of loading the specimens in a 13 mm span three-point bend from a minimum load of 50 N to a maximum load of 600–650 N at 15 Hz. This load generally resulted in the desired precrack length of approximately half the specimen thickness (*W*/2) being achieved in 30,000–50,000 cycles. Because of the extremely small specimen geometry, a gauge-free precracking method had to be employed—rather than monitoring crack growth directly, changes in displacement during cyclic loading were correlated to changes in crack length. This work found that for a specimen with an approximately nominal starter notch length, a change in peak displacement of 15–16 μm after an initial "breaking in" period of 3,000–10,000 cycles correlated to a total precrack length of approximately 2.25 mm, or *W*/2. Once the desired change in peak displacement was achieved, the maximum load was reduced such that the load amplitude was half the initial precracking step. An additional 10,000 cycles were then applied to sharpen the crack tip, ensuring maximum stress concentration.

Monotonic J–R testing was performed at room temperature as well as in the 100°C–600°C range in 100°C increments. An initial 20 N preload was applied during heating to ensure contact was maintained during thermal expansion of the load train. The specimen temperature was monitored directly via a thermocouple port in the back of the fixture. Once the specimen was within ±5C° of the nominal temperature, it was held in that range for 5 min prior to testing. The specimen was then loaded in displacement control at 0.005 mm/s until either the load had dropped to approximately half the maximum load or an excessive displacement (5+ mm) had been reached. Time, load, and displacement data were acquired at a rate of 5 Hz. If the specimen was tested at or below 300°C, it was heat-tinted at 400°C+ to mark the final crack length and manually broken in half.

The fracture surface of each specimen half was imaged using a low-magnification optical microscope, and the initial and final crack lengths were measured using a nine-point weighted average in accordance with ASTM E1820 and averaged between specimen halves. Fracture lengths were measured in pixels, then converted to millimeters using the undeformed bottom edge as a scale. With the raw load–displacement data and crack length data, the fracture resistance or J–R curve of each specimen could be constructed. Given the lack of direct crack opening measurement, the only useable calculation method was the normalization method outlined in [8]. A modified normalization method was used for this test campaign because this work found that direct application of the normalization method led to a breakdown in the calculations because of the high material ductility and very small specimen size. Although the modified method allowed for sensible J–R data to be produced, it should be noted that given the combined high material ductility and small specimen geometry, which do not allow for plane strain conditions, as well as the deviation from the ASTM E1820 method, the fracture results reported should not be used as a design basis. However, the modified normalization method has shown to be effective as a screening method and for showcasing the effects of differences in processing and environmental conditions on fracture behavior. Once the J–R curve was constructed, such as the one shown in Figure 14, the 0.1 and 0.2 mm offset *J* and *K* values could be determined:

$$K_{0.1,0.2\text{ mm}} = \left(\frac{J_{0.1,0.2\text{ mm}} \times E}{1-\nu^2}\right)^{0.5}, \tag{3}$$

where $J_{0.1,\,0.2\text{ mm}}$ $J_{0.1,0.2mm}$ are the *J* values at either the 0.1 or 0.2 mm offset intercept, *E* is the elastic modulus, and ν $\nu$is Poisson's ratio. Notably,N Equation 3 assumes plane strain conditions, although in actuality, plane strain is unlikely to have been achieved at any condition because of the small specimen

size and high material ductility. For simplicity, in the Results and Discussion section of this report, stress intensity factor K is reported as a function of temperature, with $K_{0.2mm}$ 2 mm being preferred over $K_{0.1mm}$ 1 mm because the scattering between data points tends to be less for the former. although

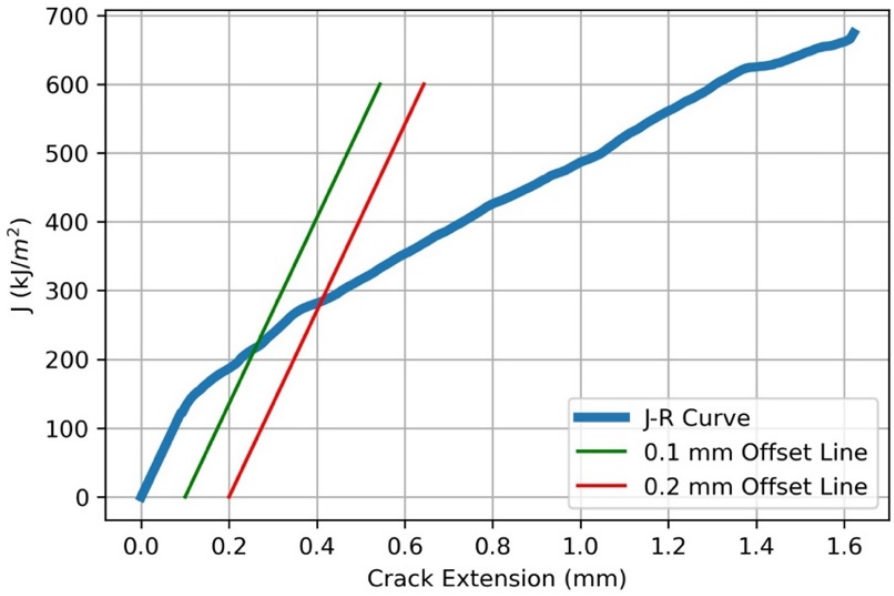

Figure 14. Example J–R curve showing the 0.1 and 0.2 mm offset lines. The offset line slopes are the same as the slope of the blunting region of the J–R curve.RESULTS AND DISCUSSION

3.1 PEREGRINE EVALUATIONS OF BUILD QUALITY

A key factor in the AMMT program's ability to accelerate the qualification timeline for additively manufactured components requires leveraging in situ process monitoring to evaluate potential build defects or identify optimized processing regimes. To date, the program has made significant progress in this space. For every build summarized in this report, at least some fraction of in situ process monitoring data exists. Some builds have in situ data over the entire build duration, and some builds had some interruptions that caused the loss of some in situ data. This section summarizes the in situ data generated for the three large Concept Laser builds shown in Figure 4 that have been used for FY 2023 and FY 2024 campaign creep testing from ORNL.

An upgraded visible light camera was installed in late August through early September 2023 improved the pixel resolution from a pixel size of 133 µm to 86 µm. As a result, build comparisons at different pixel sizes cannot be accurately represented (Tensile Blocks 01 and 02 to their respective repeats). Figure 15 shows a build-to-build comparison of the spatter detections as a function of build height. Both spikes for single layers from builds 01 Repeat and 02 Repeat are false positives. The increase around 4 mm from Tensile Blocks 01 Repeat (shown in blue) is a false detection owing to mistiming- of data, which captured an image while the laser was actively melting, and the increase around 83 mm for Tensile Blocks 02 Repeat (shown in red) captured an image of the recoater in frame. The overall trend over spatter detections, however, can be taken as true as a result of differences in volumetric energy densities for these builds.

Figure 16 showsshows a heat map of the spatter anomaly class detections. Spatter is an inherent by-product of any welding process and is common in LPBF as finer, darker particles, which are generally carried away by the flow of Ar across the build plate. However, larger spatter particles can be heavy

enough to land in the powder bed and are often remelted into the final component. On a per-part basis, the maximum detections for spatter were 3.7%, 0.7%, and 7.0% for builds 01 Repeat, 02 Repeat, and 04, respectively. The VED for these builds were 71, 52, and 135 J/mm^3, respectively, and an increase in spatter detections occurred with increasing VED. Because spatter particles can result in lack-of-fusion pores, it is worth maintaining a low VED to minimize process effects on other printed components.

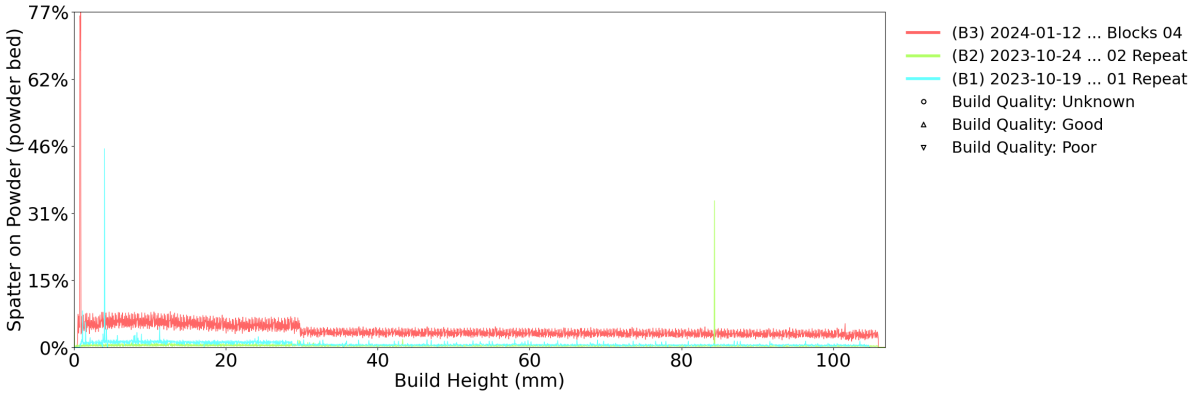

Figure 15. A comparison of spatter of tensile block builds on the Concept Laser M2.

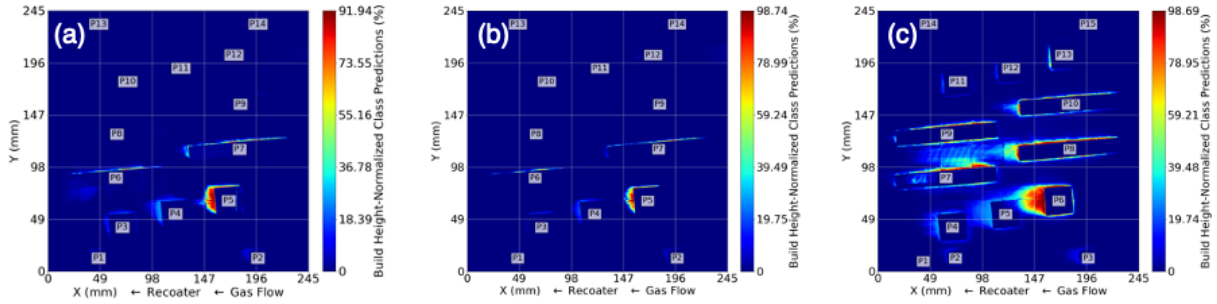

Figure 16. Spatter on powder detections for (a) Tensile Blocks 01 Repeat, (b) Tensile Blocks 02 Repeat, and (c) Tensile Blocks 04. These builds correspond to equivalent VEDs of 71, 52, and 135 J/mm^3, respectively.

Figure 17 showsshows a build-to-build comparison of the overmelting detections as a function of build height. Overmelting is a common class detection when the nNIR sensor is nearly or completely oversaturated with detected photons. This oversaturation is more likely with parts that appear hotter when melted with higher VEDs. This trend was expected given that the VED for these builds were 71, 52, and 135 J/mm^3 for builds 01 Repeat, 02 Repeat, and 04, respectively.

Figure 18 shows a heat map of overmelting anomaly class detections summed through the build height (*Z*). Overmelting is noticed as pixels that appear relatively brighter for large areas of printed material, which often contribute to swelling or superelevation detections. Disregarding Zeiss ParAM coupons, the maximum detections for overmelting are 77.7%, 20.7%, and 96.2% for 01 Repeat, 02 Repeat, and 04, respectively. Moreover, the average detections for these builds is 38.8%, 16.7%, and 74.7%, respectively. Despite showing a large number of overmelting detections at higher VED, melting at higher VED can be beneficial for healing previous layers' flaws because of the lack of fusion. Despite this possibility of healing, there is an increased likelihood of inducing keyholing subsurface flaws.

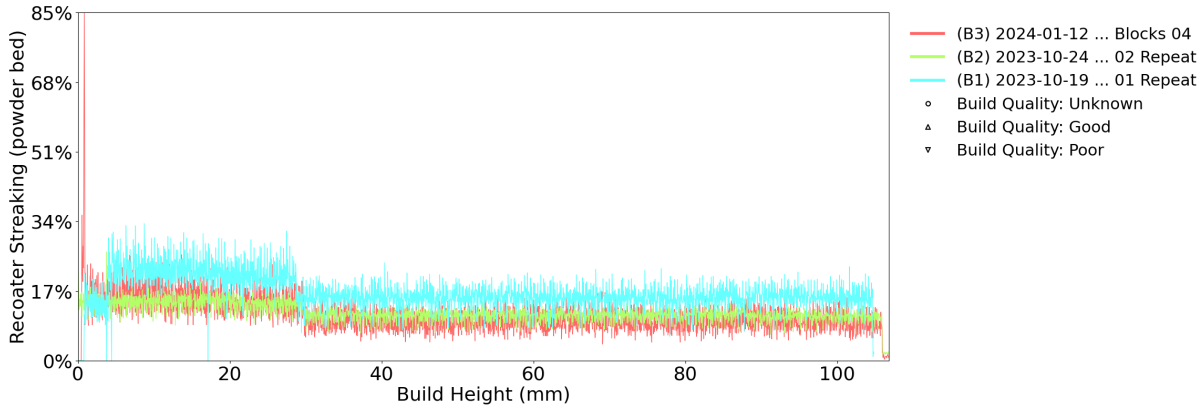

Figure 17. A comparison of overmelting detections of tensile block builds on the Concept Laser M2.

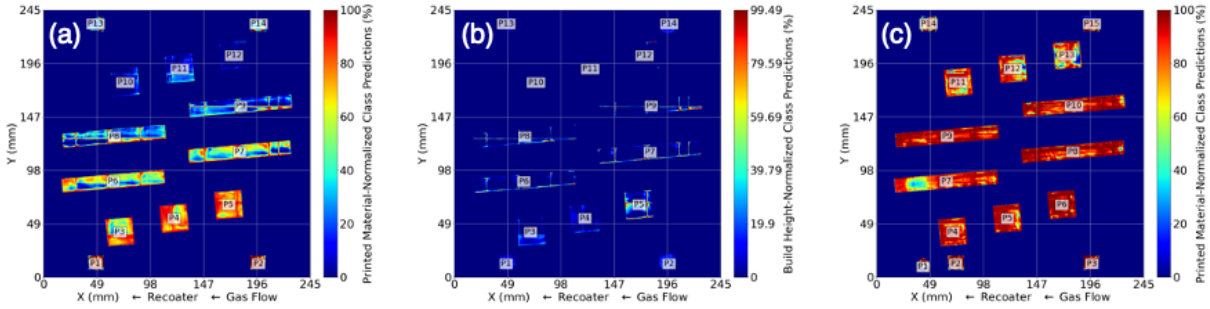

Figure 18. Overmelting detections normalized by printed material for Tensile Blocks (a) 01 Repeat, (b) 02 Repeat, and (c) 04. These samples correspond to equivalent VEDs of 71, 52, and 135 J/mm^3, respectively.

Figure 19 shows a build-to-build comparison of the recoater streaking detections as a function of build height. *Recoater streaking* is when the recoating mechanism—a rubber wiper in this case—is damaged slightly and causes streaks in the direction of powder spreading. It can also occur when larger spatter particles or debris are pushed along the length of the powder bed. Note that recoater streaking did not increase with increasing VED. Possible reasons for this are that higher VEDs often result in a high surface roughness but do not necessarily generate a sharper edge of parts that are responsible for recoater streaking. Regions of high recoater streaking may be susceptible to flaw generation. Figure 20 shows a heat map of recoater streaking detections for each tensile block build. The maximum recoater streaking detections were 53.2% for Tensile Blocks 01 Repeat, 34.9% for Tensile Blocks 02 Repeat, and 37.9% for Tensile Blocks 04. The average recoater streaking detections were 217%, 15.1%, and 17.9%, respectively.

The results of these analyses show that some factors can be detected and linked to properties, such as solidification velocity or VED. Future work will aim to link these signatures with performance metrics registered to spatial build coordinates.

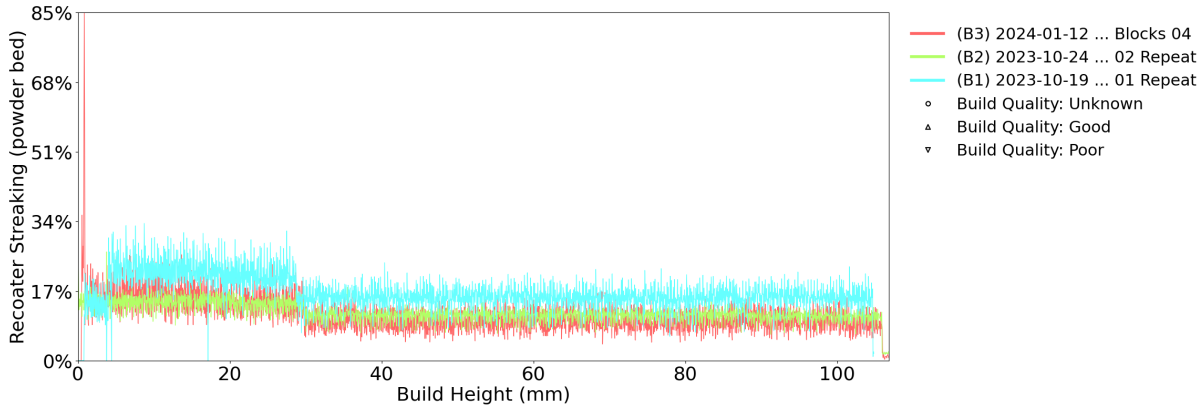

Figure 19. A comparison of recoater streaking detections of tensile block builds on the Concept Laser M2.

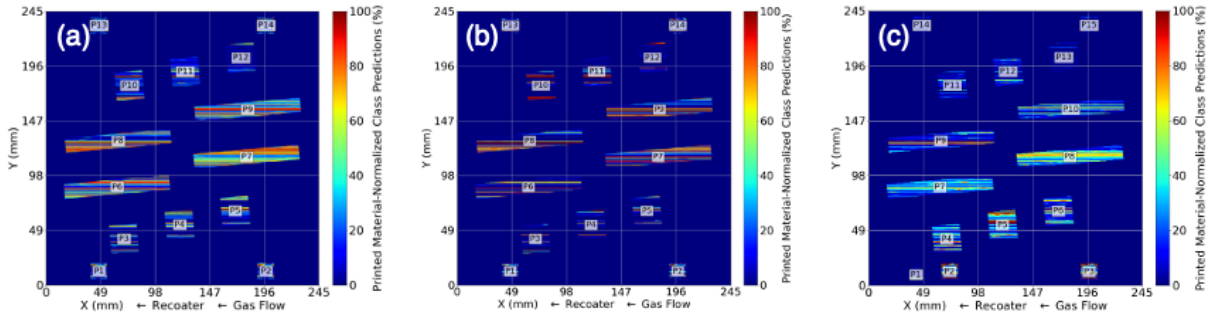

Figure 20. Recoater streaking detections summed through *Z* for Tensile Blocks (a) 01 Repeat, (b) 02 Repeat, and (c) 04. These samples correspond to equivalent VEDs of 71, 52, and 135 J/mm^3, respectively.

3.2 SCALED BUILD EVALUATIONS

3.2.1 Concept Laser Builds

To date, XCT data have been collected on Zeiss samples, subsized tensile specimens (SSJ2s), and -full-sized creep and creep-fatigue specimens built using the GE Concept Laser. Although specimens that were printed on the Renishaw AM400 have been scanned, that data will be presented in a subsequent section. A summary of the concept laser data is shown in Figure 21. Although the data comprise two different build processing parameters (builds Tensile Blocks 01 and 02), the data show very specific trends. The color of the data points represents the chosen HT (see Table 5). Generally, the SR and SA conditions showed larger porosity levels, and the HIP porosity decreased as expected.

The data begin to diverge when looking at the measured XCT porosity levels as a function of the specimen type (marker style in Figure 21). For instance, for the Zeiss cylinder, creep, and fatigue specimens, the data show less than 0.1% porosity, and is higher variance appears for the SSJ2 specimens. Although the SSJ specimens were smaller in size, the scanned voxel resolution was similar for these scans vs. the creep or creep-fatigue specimens, so the large difference in porosity either is suspect between these data points or some --part-to-part heterogeneity exists. After scanning the creep and creep-fatigue specimens, the newly machined holder was found to provide different background noise when the x-rays attenuated through the holder vs. the region of the gauge protruding from the holder. This difference in contrast resulted in a poorer detection efficiency and minimum detectable pore resolution for the creep and fatigue specimens vs. the SSJ specimens. As such, the SSJ data in this figure are likely more representative of the porosity levels in the creep and fatigue specimens tested in the first round of AMMT program creep and fatigue testing.

The same trend was shownis apparent as a function of process parameters. For the Tensile Blocks 01 build (~0.03% porosity), the variance shown with HTs and specimen type plotted in Figure 22 is within the margin of error. However, for Tensile Blocks 02 (~0.3%–0.4% porosity), the SSJ specimens were capable of identifying the porosity, but the creep specimens were unable to do so. This trend is expected to be resolved in future XCT scans because a new creep and fatigue specimen holder has been designed that prevents shadowing.

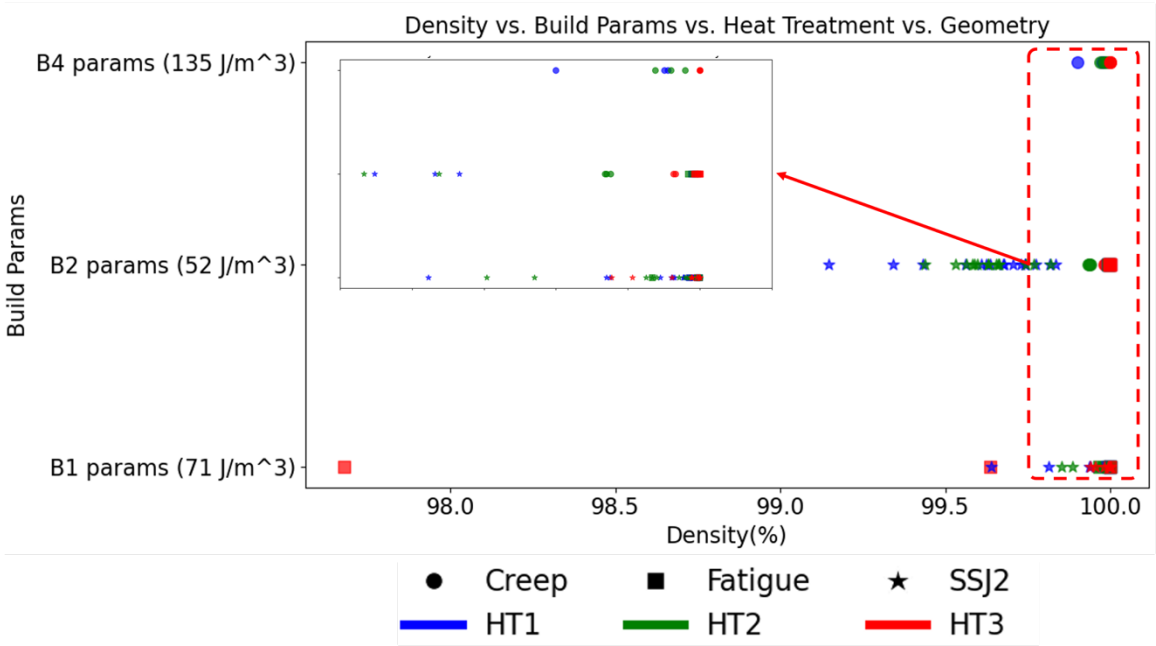

Figure 21. Comparison of all geometries: impact of HT and build parameters (B1: Tensile B01, B2: Tensile B02, B3: Tensile B03, B4: Tensile B04). HT1: SR, HT2: SA, HT3: HIP. For B3, good agreement was observed between creep samples and the cylindrical part of Zeiss geometry. For B1 and B2, the observation is similar to what was observed in Figure 9 for SSJ2 samples. The fatigue sample, however, showed differences, which is still being investigated.

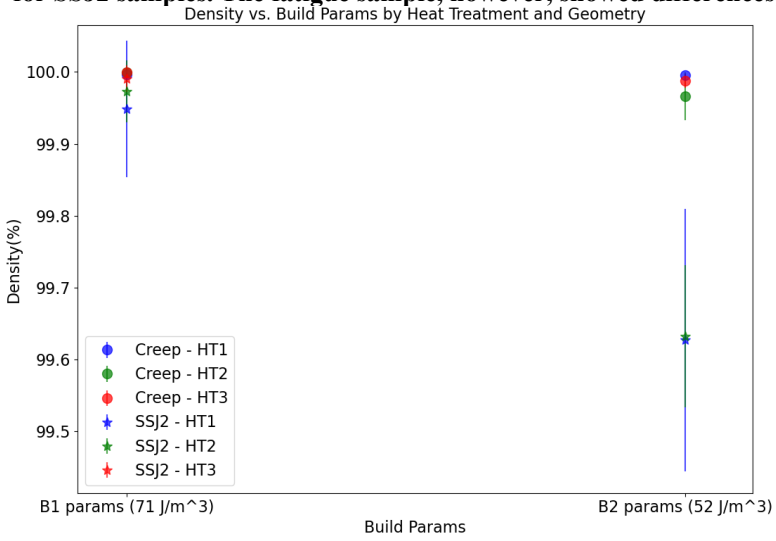

Figure 22. Comparison of SSJ2 and creep samples: impact of HT and build parameters (B1: Tensile B01, B2: Tensile B02). HT1: SR, HT2: SA, HT3: HIP. The error bar for creep samples is based on the average of 6 coupons (HT1-B1, HT2-B1) and 3 coupons (HT3-B1, HT1-B2, HT2-B2, HT3-B2); for SSJ2s, it is the average of 16 coupons for each scenario. For B1 parameters, good agreement occurred between SSJ2 and creep data, especially for the HT2 and HT3 cases. However, for B2 parameters, the trend is quite different, and the results do not align very well.

The differences between Tensile Blocks 01 and Tensile Blocks 02 (the two builds from which specimens were harvested initially for irradiation and mechanical testing) are highlighted in Figure 23. Not only are the differences in porosity evident between the two builds, reinforced from prior XCT analysis, but differences in grain structure also appeared. The lower VED build, Tensile Blocks 02, had a finer grain size with a marginally smaller grain aspect ratio. Although the grains remained somewhat columnar, the grain morphology of the Tensile Blocks 02 build was more chevron-shaped. Conversely, the Tensile Blocks 01 build had were a more columnar grain structure, as shown by the increase in average grain size and aspect ratio. Even with this change in grain size, these results show a benefit of significantly less lack-of-fusion porosity in the slightly higher VED build (Tensile Blocks 01).

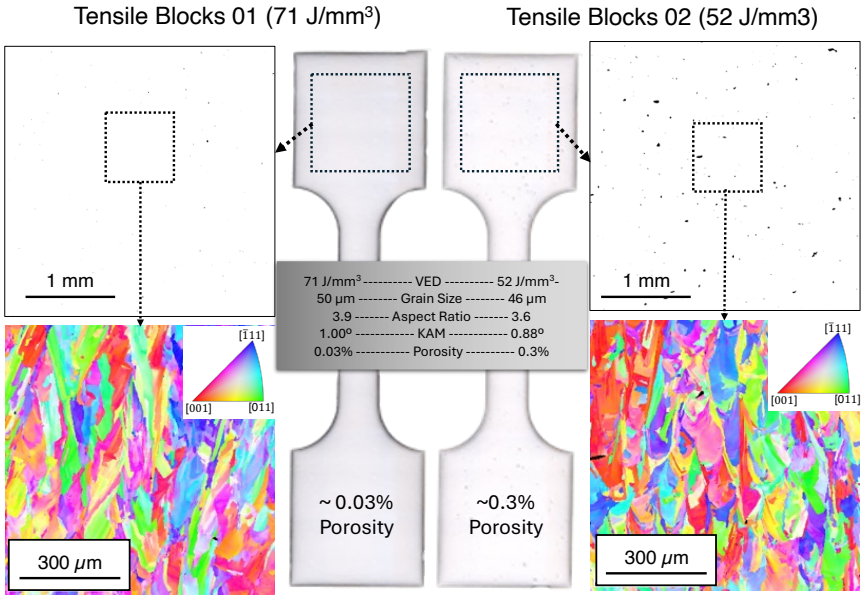

Figure 23. EBSD inverse pole figure maps and optical porosity images of representative SSJ2 specimens machined from (left) Tensile Blocks 01 and (right) Tensile Blocks 02.

In FY 2023, a significant assumption in the use of the miniature Zeiss specimen for high-throughput optimization was that the small specimen (15 mm in diameter and total height) could be representative of the microstructure within the larger plate builds for witness specimen testing. This FY, scaling builds enabled the comparison of microstructures in different part geometries. From Tensile Blocks 01 and Tensile Blocks 02 builds, Zeiss specimen geometries were compared with specimens extracted from the tall, rectangular plates and the cubes printed on the same baseplate subjected to identical HTs.

One such comparison is shown in Figure 24 for Tensile Blocks 01 specimens in the SR and SA conditions. The grain structure, which consisted of elongated columnar grains oriented parallel to the build direction, was identical for all three samples. The similarity in grain structure does not fully guarantee identical nanoscale precipitation or chemical segregation behavior, but subsequent mechanical testing data (highlighted in Figure 25) show identical strain hardening and strength values for tensile specimens extracted from the same plate and cube materials shown here. Unfortunately, the Zeiss specimen data are not shown here because the tensile tests in Figure 25 were collected in the build direction, but the FY 2023 data on Zeiss mechanical tests were collected in the transverse orientation. The similarity in microstructure for the Zeiss specimen nevertheless provides strong evidence that this geometrically complex high-throughput design can continue to be used for not only 316H SS but also other materials as LPBF research continues for accelerated qualification initiatives.

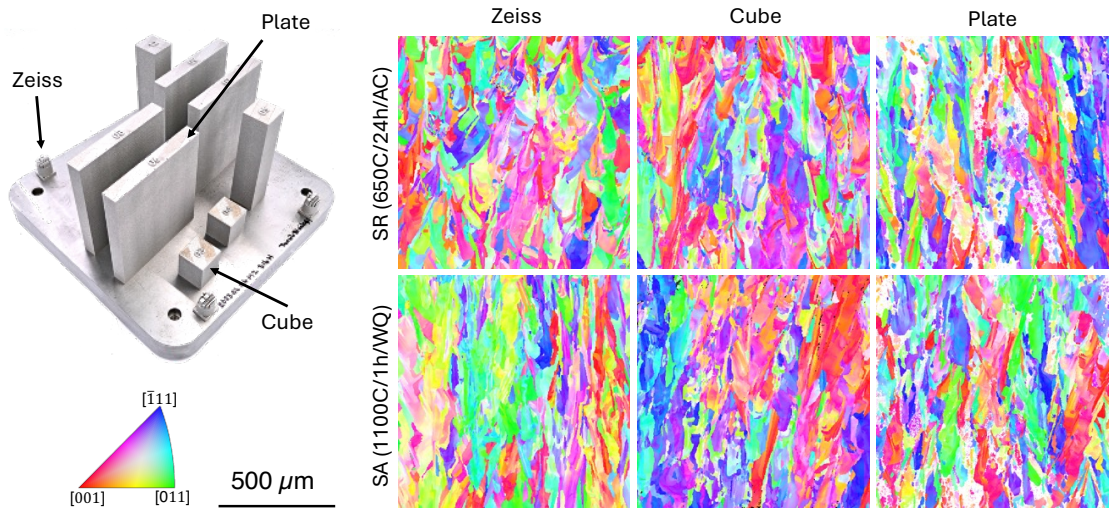

Figure 24. EBSD inverse pole figure maps of Tensile Blocks 01 grain structures for varying geometries.

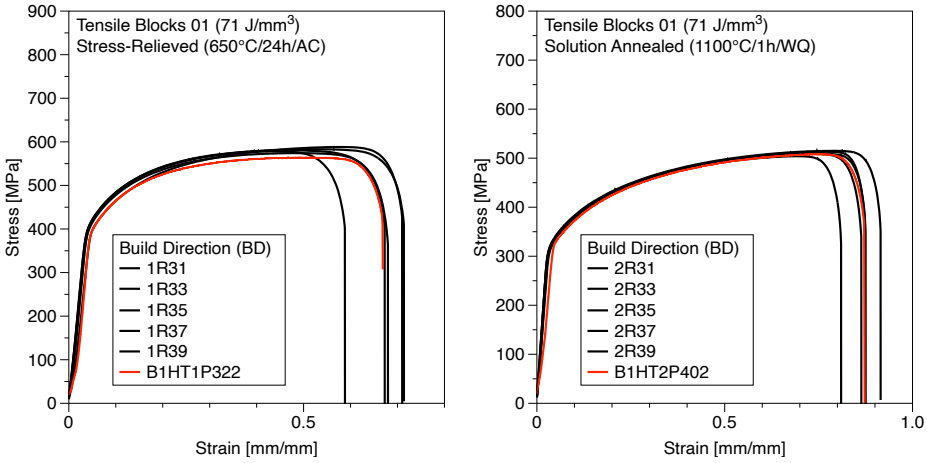

Figure 25. Engineering stress–strain tensile curves for subsized tensile specimens extracted from (black) larger plate and (red) cube parts from the larger Tensile Blocks 01 build.

The lack of heterogeneity in the tensile data is reinforced by a detailed analysis of the variation of microstructure along the build height of an SR Tensile Blocks 01 part. The as-deposited builds are known to have anisotropy in their structure because the directional building process introduces variation in part properties. During the building process, the heat flow progresses from the first to last layers of the builds and causes property variations such as differences in the parts' mechanical and microstructural properties. One reason for this variation is a lowered cooling rate with increased build height because of the heat input accumulation toward to the top of the build [9, 10]. This result was proved by measuring the infrared camera signals along the 113 mm tall parts that were LPBF-processed between 49 and 81 J/mm^3, which showed the highest signal counts and deeper melt pools toward the top of the builds [10].

The build height effect on SR samples are shown in Figure 26 and Figure 27. To reveal the property variations along the build directions, Tensile Blocks 01 (B1, 71 J/mm^3) and Tensile Blocks 02 (B2, 51 J/mm^3) were equally sectioned into three subsamples, which were called *top* (i.e., top of the build), *middle*, and *bottom*. Those samples were further divided into two parts to capture the surfaces along build

(*XZ*) and deposition (*XY*) directions. Figure 26 and Figure 27 show the collected EBSD maps and grain size statistics from those surfaces. According to these figures, in both builds, grains at *XZ* surfaces were longer than the *XY* surfaces because of epitaxial growth through multiple melt pools along the build direction. The B2 build grains along the *XZ* direction were generally randomly oriented with between 1.7 and 3 texture intensities, and their long axis size and aspect ratios ranged from, on average, 24 to 29 μm and 3.3 to 3.8, respectively. B2 build grains along *XY* direction also displayed a similar structure, and their orientations were also randomly oriented between 1.3 and 1.4 texture intensities. Their grains' long axis and aspect ratios were measured from 16.5 to 19 μm and 2.3 to 2.5, respectively, which were more equiaxed than the *XZ* surface's grains. The difference in the build height seemed to have no effect on either the orientation or grain sizes of both surfaces of the B1 build and showed very similar measurements of grain size. The grain of the B1 build along *XZ* had a slightly stronger texture along the <001> direction—between 2.5 and 5 intensity—compared with the B2 *XZ* surface grains, and the texture was shifted from the <001> to the <111> direction when the scan was moved from the bottom to the top of the builds. The grains' long axis and aspect ratios were measured from 31 to 36 μm and 4.2 to 4.5, respectively, which were slightly longer than the B2 *XZ* surface grains. The grains along the *XY* direction showed a more equiaxed structure, similar to theB2 *XY* plane, and their textures were closer to the <011> direction with 2.5–6.5 texture intensity. This result shows that with increased energy density, the texture properties along the *XY* direction were more pronounced than low–energy density (B2) builds. The grain size of the B1 *XY* surface was slightly coarser than the B2 *XY* grains and measured between 17 and 20 μm with an aspect ratio of 2.3–2.5. The difference in the build height seemed to have no effect on either the orientation or grain sizes of both surfaces of the B1 and B2 build. This study can conclude that the parts produced between 51 and 71 J/mm^3 at a 100 mm height did not show significant variation in their microstructural properties across the different build height. This result is consistent with Chniouel et al.'s work [11], which reported uniform grain lengths at different build heights for 316L SS builds.

The effect of different build height on hardness properties were given in Figure 28 and according to that, the hardness of B1 samples along XY direction is slightly lowered from 211±7 to 203±6 HV, while B2 samples showed an opposite trend and slightly increased from 205±7 to 213±8 HV, when indentation area was moved from bottom to top of the build. The discrepancy in the trends could be caused by different porosity levels in both builds which can affect the hardness properties. The XZ surface of B1 samples is measured between 210±5 and 222±7 HV, while B2 XZ plane is measured between 212±4 to 207±11 HV from bottom to top.

From the hardness measurements, the builds do not show a significant variation at different build heights. The properties of the different surfaces are also similar which implies that the hardness properties are uniform across the different build heights and different surfaces. We could conclude that the parts produced between 51-71 J/mm^3 at 100mm have uniform hardness properties across different build height and planes. This result is consistent with Chniouel [11] where the hardness of L-PBF 316L parts printed on a room temperature substrate averaged 232-35HV along 80mm build height. Mohr et al [10], reported very subtle hardness loss from lower to the higher parts of a 113mm tall build, L-PBF processed between 49-81 J/mm^3. These results indicate that, the hardness variation in L-BF processed builds, under 120mm height, does not have significant variation along the build height. While this statement contrasts with directed energy deposition (DED).powder with DED between 12-20 J/mm^3 energy densities and reported lowered hardness from 198 to 183 HV within 10 mm distance along the build height in 20 J/mm^3 samples, but reported a consistent hardness ~205 HV at 12 J/mm^3 energy density. The significant variations in hardness within shorts span most likely caused by DED method production when compared with L-PBF method. Therefore it can be concluded that L-PBF processed parts produce more uniform hardness properties in a different build heights than the DED processed samples.

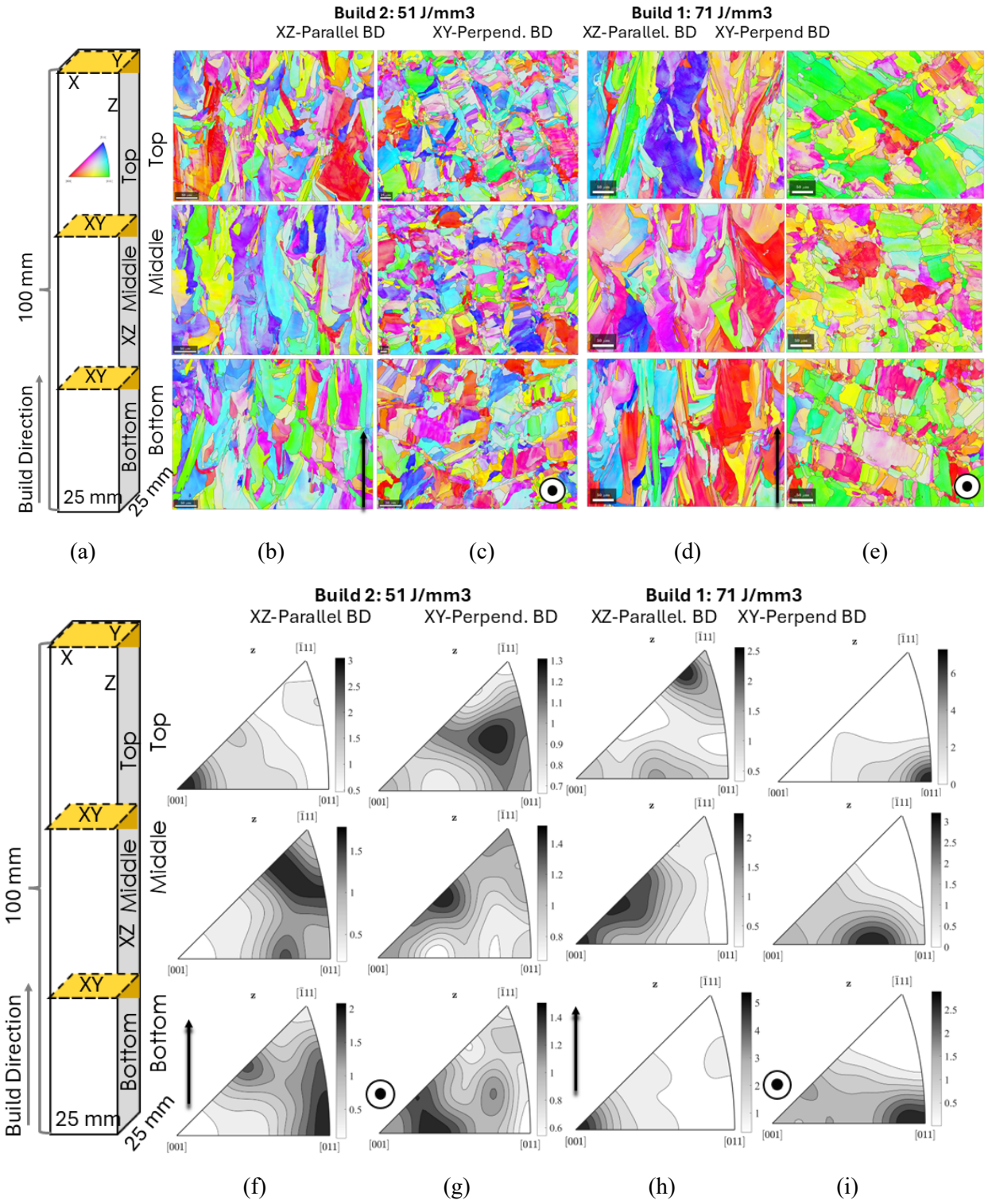

Figure 26. 316H SS samples were (a) sectioned into three subsamples as shown in the schematics. The surfaces at the (b, d, f, h) *XY* plane (perpendicular to build direction) and (c, e, g, i) *XZ* plane parallel to the build direction were scanned with the EBSD method. The samples were printedas (b, c, f, g) 51 J/mm^3 Build 2 and (d, e, h, i) 71 J/mm^3 Build 2, subsequently stress-relieved at 650°C for 24 h, and air-cooled. The orientation maps were given between (b) and (e), and their corresponding inverse pole figure triangles were

shown between (f) and (i). The corresponding locations of the maps on the builds were indicated as the top, middle, and bottom on the schematics.

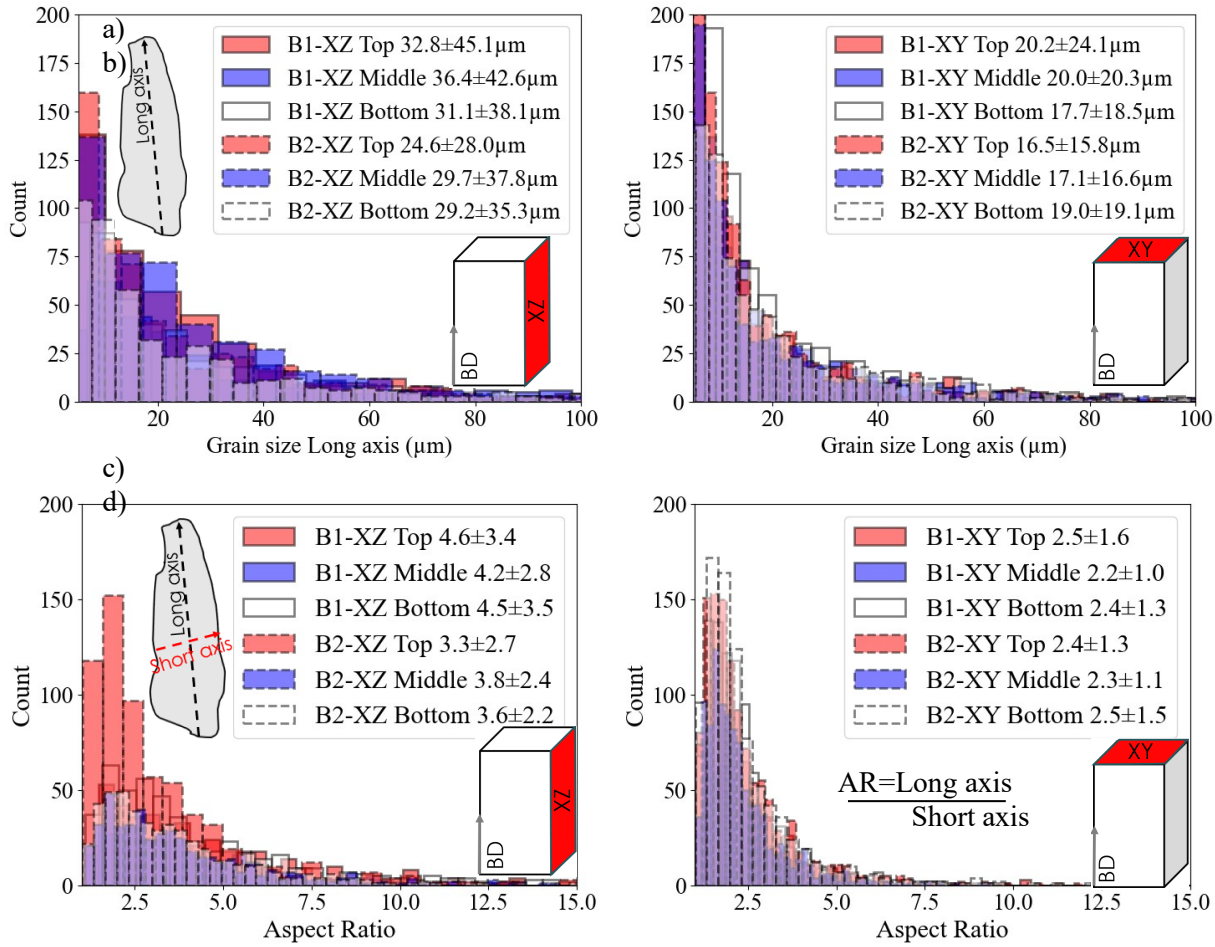

Figure 27. Sectioned 316H SS builds for the (a, c) *XZ* and (b, d) *XY* planes' grain size measurements represented with (a, b) the grain's long axis and (c, d) aspect ratios of the grain sizes. The corresponding build surfaces were highlighted on the inset schematics in red. The grain's long and short axes were indicated on the other inset figures within the images.The effects of different build heights on hardness properties are given in Figure 28, and according to those effects, the hardness of B1 samples along the *XY* direction is slightly lowered from 211 ± 7 to 203 ± 6 HV (Vickers hardness), but the B2 samples showed an opposite trend and slightly increased from 205 ± 7 to 213 ± 8 HV, when the indentation area was moved from the bottom to the top of the build. The discrepancy in the trends could be caused by different porosity levels in both builds, which can affect the hardness properties. The *XZ* surface of B1 samples was measured between 210 ± 5 and 222 ± 7 HV, and the B2 *XZ* plane was measured between 212 ± 4 to 207 ± 11 HV from bottom to top.

As evidenced from the hardness measurements, the builds did not show significant variation at different build heights. The properties of the different surfaces were also very close, which implies that the hardness properties were uniform across the different build heights and different surfaces. This study can conclude that the parts produced between 51 and 71 J/mm^3 at 100 mm have uniform hardness properties across different build heights and planes. This result complies with Chniouel's [11] result in which researchers measured the hardness of the parts LPBF-printed on a room-temperature substrate with an average 232–235 HV along the 80 mm build height for 316L SS parts that were built. Mohr et al. [10]

reported very subtle hardness loss from lower to higher parts of the 113 mm tall build that was LPBF-processed between 49 and 81 J/mm^3. These results indicated that the hardness variation in LPBF-processed builds under 120 mm in height did not have significant variation along the build height. However, this statement contrasts with different DED. Chechik et al. [12] printed 316H SS powder with the DED method between energy densities of 12 and 20 J/mm^3 and reported lowered hardness from 198 to 183 HV within 10 mm distance along the build height in 20 J/mm^3 samples, whereas they reported a consistent hardness of approximately 205 HV at an energy density of 12 J/mm^3. The significant variations in hardness within short spans was most likely caused by using the DED method of production when compared with the LPBF method. Therefore, this comparison can conlude that LPBF-processed parts produce more uniform hardness properties in different build heights than the DED-processed samples.

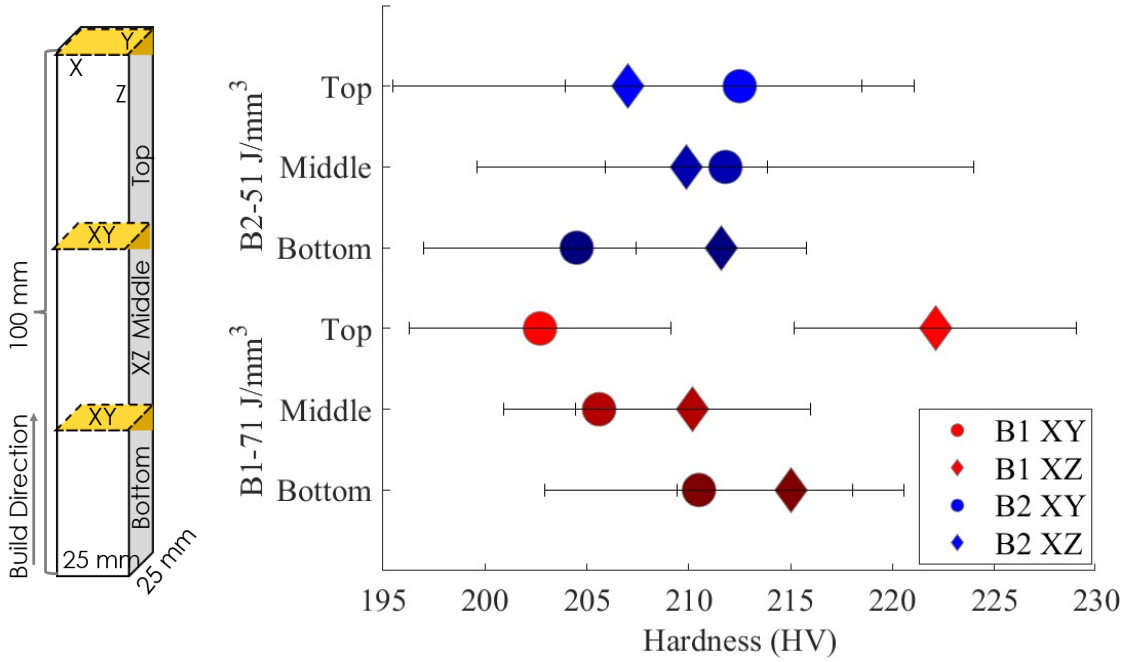

Figure 28. Hardness values of the measured SR parts. The *XZ* (along build direction) plane is represented with diamond, and the circle indicates the *XY* plane. **Renishaw Build Comparisons**

In FY 2024, multiple larger builds were completed on the Renishaw system at ORNL, spanning processing parameters deemed to have minimal porosity by both ANL and ORNL during parallel process optimization efforts. All builds were completed with Praxair Lot 2 powder (0.06% C), and both processing parameters were printed within the same build(s).

To evaluate the difference in porosity between the two builds, both optical microscopy and XCT were performed. XCT analysis was performed on creep and fatigue specimens using the new holder without background correction issues highlighted previously for the Concept Laser specimens. XCT porosity results are provided in Figure 29, which compare the porosity distributions in ORNL-printed variants of either the ANL-recommended or ORNL-recommended parameters. Two ANL-parameter plates were printed and heat-treated to HT1 and HT2 conditions, data point does not exist. For the HT1 and HT2 conditions, the results show a higher average density for the ANL-recommended parameters vs. the ORNL-recommended parameters based on a paired two-tailed T-test on the two porosity sample distributions ($p<0.07$).

Going forward, if additional specimens will be printed by ORNL, a new set of ORNL-optimized parameters will likely be chosen because of recent updates to the machine learning algorithm being used

to analyze the existing XCT data. For example, the current "ORNL-Best" parameters printed in this work, when using the FY 2023 version of the XCT algorithm, estimated density to be 99.9% in the Ziess specimens, but a new analysis of the data in FY 2024 showed only 99.6% density for the exact same scan data. This result indicates that at least some additional optimization may be needed to minimize porosity for the ORNL builds on the Renishaw AM400.

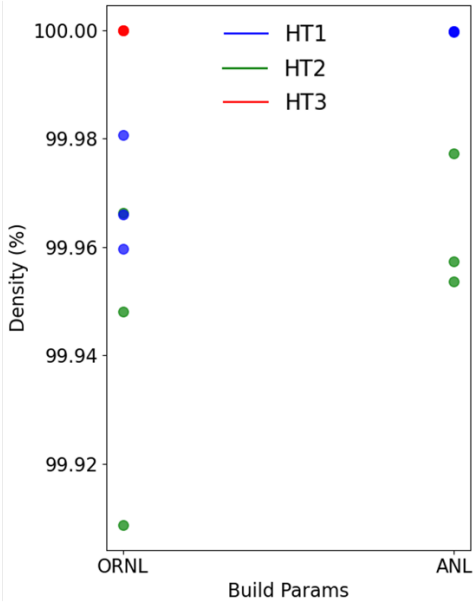

Figure 29. Comparison of ANL-best vs. ORNL-best creep specimen. Build-parameter vs. HT vs. density. B1 params: Best-01, B2-params: Best-02 and B3 params: Best-03. ANL only had results for B2-param at two separate HTs and, it seems, overall performed slightly better than ORNL-Best for those cases. In each scenario, three samples were scanned, some of which were overlapping at approximately 100% density. For optical microscopy and EBSD analysis, a small section of each large plate was mounted and polished to a colloidal silica finish, followed by porosity analysis using the ImageJ software package. In addition to builds performed at ORNL, ANL sent a plate of their own round-robin build for microstructure comparison. These specimens were all in the as-built condition, although the three HT parameters used in this work were not expected to significantly influence the grain size distributions.

In Figure 30, the EBSD inverse pole figure maps are shown at the same magnification for the ANL-provided plate and the two ORNL-produced plates. The ANL and ORNL plates printed using the ANL-recommended printing parameters (lower equivalent VED of ~53 J/mm^3) have grains described here as having a characteristic chevron-style morphology, whereby the grain structures solidify into more refined grains that emulate the shape of the prior solidifying melt pool. Although the average area weighted circular equivalent grain size of the ANL plate was marginally smaller than the ORNL plate, the difference remained within the margin of error for the grain size distributions. Conversely, the ORNL plate printed with the higher VED of approximately 76 J/mm^3 began to show the characteristic coarsening of the grain structure (with the average grain size doubling in comparison with the lower-VED variant) into larger columnar grains oriented vertically (aligned with the build direction).

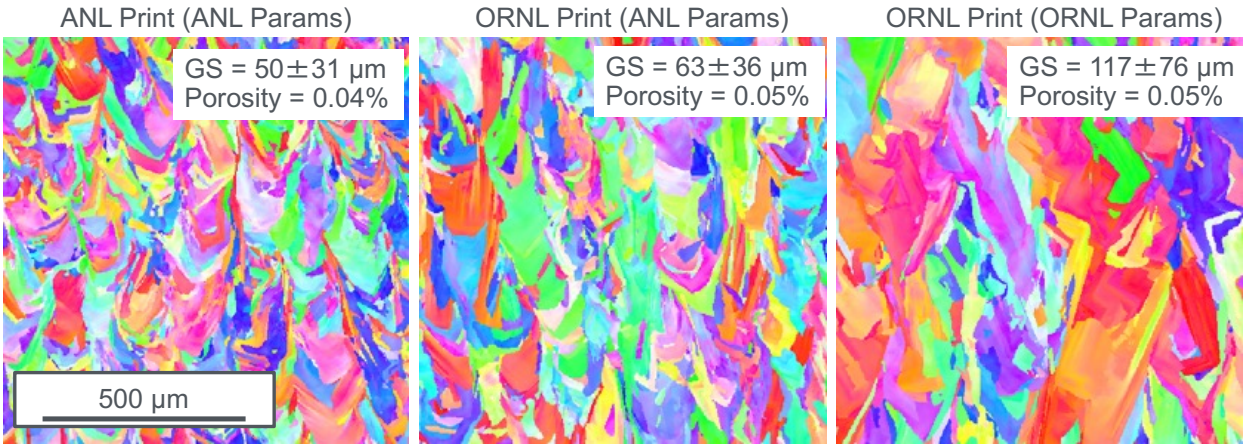

Figure 30. EBSD inverse pole figure maps of ANL-printed and ORNL-printed Renishaw builds. The inverse pole figure legend is identical to that shown in Figure 24.EOS Build Characterization

In July 2024, ORNL successfully completed a round-robin build on the ORNL EOS M290 system, replicating a prior print performed by LANL earlier in the fiscal year, albeit on Praxair Lot 4 powder at ORNL (0.07% C) vs. the use of the PAC lot of powder (0.04% C) at LANL. Since this build, LANL has replicated additional builds using the Praxair Lot 4 powder used here, which allows for a 1:1 comparison between LANL and ORNL builds using this system with identical powder lots.

Although additional characterization will occur in FY 2025 as a prerequisite to neutron irradiation, preliminary optical and EBSD characterization was completed this year to assess differences in grain size and morphology in comparison with ORNL concept laser prints because both use a continuous laser in comparison with the pulsed-laser Renishaw builds. Representative microstructural features are illustrated in Figure 31, showing a larger grain size in comparison with the concept laser Tensile Blocks 01 build and have a similar columnar grain morphology. The porosity was also very low for the specimen analyzed, measuring approximately 0.09% in the as-built form. The minimal porosity was more spherical in nature, which is consistent with slight keyholing at this print condition, which is another similarity with the higher-VED Concept Laser build.

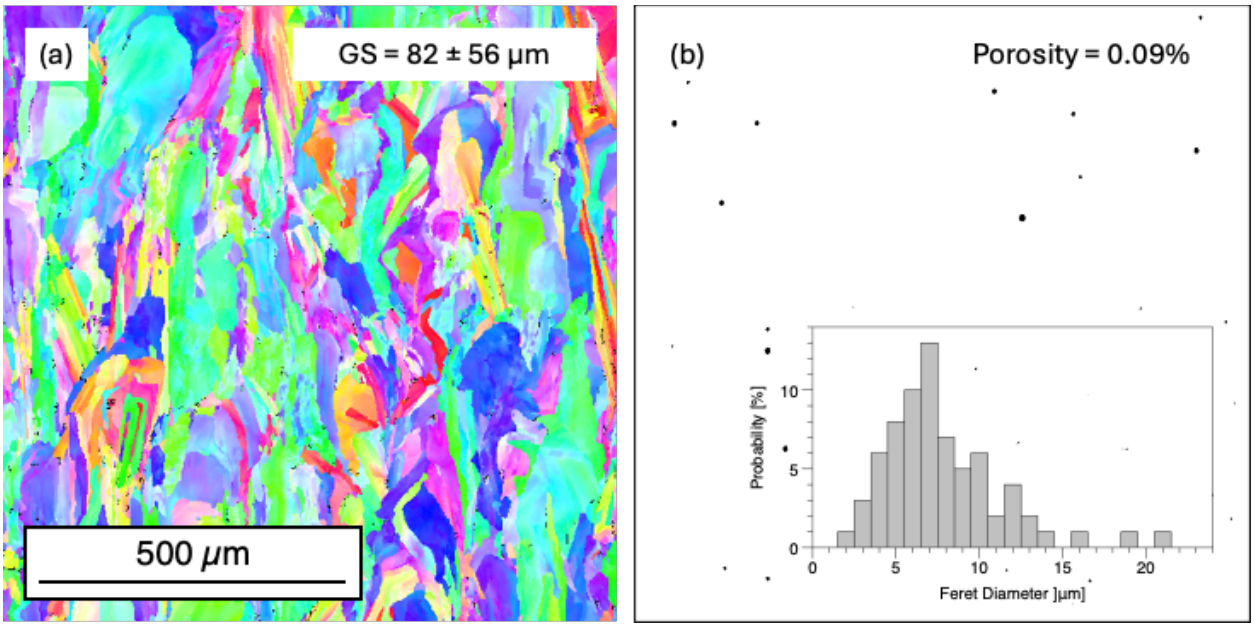

Figure 31. (a) EBSD inverse pole figure map and (b) optical porosity analysis of ORNL-printed EOS M290 build using Praxair Lot 4 (0.07% C) powder. The inverse pole figure legend is identical to that shown in Figure 24.HEAT TREATMENT AND PROCESSING EFFECTS ON TIME-INDEPENDENT MECHANICAL PROPERTIES

Significant data have been generated this year on both the time-independent properties (tensile and fracture toughness) and time-dependent properties (creep and creep-fatigue) for various LPBF 316H SS builds in the AMMT program. Because the time-dependent properties have been summarized in a parallel report [7], only the time-independent properties of select builds will be presented in this section. Regardless, many of the same trends in performance data are echoed in both the time-dependent and time-independent data.

High-temperature tensile tests were performed on both the Tensile Blocks 01 and Tensile Blocks 02 builds up to a test temperature of 600°C. Because the trends were similar for both builds, for brevity, only the tensile data for Tensile Blocks 01 is presented here, but the data for Tensile Blocks 02 is available upon request. Specimens were tested in both the transverse direction and the build direction to assess the degree of anisotropy as a function of test temperature. Additionally, all three HT conditions (Table 5) were tested.

Plots of the yield strength, ultimate tensile strength, uniform elongation, and total elongation are provided in Figure 32, overlaying effects of both specimen orientation and HT simultaneously. A clear effect of the HT condition occurred on the tensile properties. As the HT became more rigorous, increasing in temperature from 650°C (SR) to 1,100°C (SA) and to 1,150°C (HIP), the average yield strength and ultimate tensile strength decreased, with the largest difference being at room temperature. However, the degree of difference between the various HTs decreased as test temperature increased. At room temperature, a 100 MPa difference in strength was shown between the SR condition and the SA/HIP conditions, but at 600°C, this difference was minimal. Thus, depending on the application temperature expected for the LPBF 316H SS component, the SR condition does not clearly provide significant benefits in high-temperature strength. Additionally, the SR condition comes with a significant reduction in strain hardening capacity at high temperatures, as shown by the very low uniform elongation of the SR condition at 600°C.

Generally, the build direction showed higher ductility and lower strength in comparison with specimens loaded in the transverse direction [TD]. This trend was noted for both the Tensile Blocks 01 build shown in the figure as well as with the lower-VED Tensile Blocks 02 build because of similar levels of preferred grain textures developed during the AM process. This anisotropy is quite severe, particularly with respect to ductility at lower temperatures, but at 600°C, the degree of anisotropy related to strength and ductility seemed to decrease. Additional data are needed to fully quantify the dependence of time-dependent and time-independent data as a function of loading orientation.

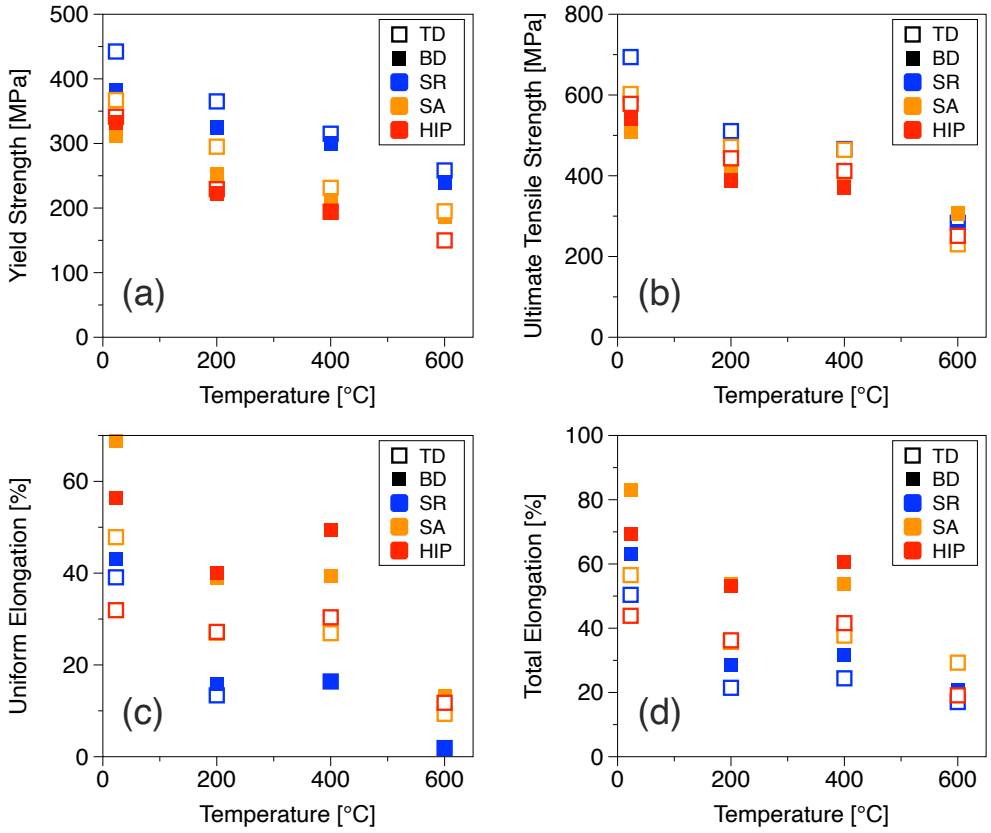

Figure 32. Tensile properties of LPBF 316H SS (Tensile Blocks 01, 71 J/mm^3) tested from 23°C to 600°C.

In addition to notable effects of HTs on the tensile properties of the concept laser prints, significant differences occurred in fracture toughness for the LPBF 316H SS specimens printed on the concept laser as a function of HT and processing condition. Because of the notable differences in performance between the lower-VED (Tensile Blocks 02, 52 J/mm^3) and the higher-VED (Tensile Blocks 01, 71 J/mm^3) prints, fracture toughness plots were created and are shown for both builds in Figure 33. Generally, the fracture toughness increases with more rigorous HTs (higher heat treatment temperatures), with the lowest fracture toughness being observed in the SR condition for both builds and the highest for the HIP treatment. In all conditions, the wrought reference material had higher fracture toughness at all temperatures, although data points at lower temperatures are expected to significantly overestimate the actual fracture toughness of the material because of its very high ductility, which causes a deviation from the plane-strain assumption during data analysis. As such, data points with abnormally high fracture toughness values (>400 MPa $\sqrt{m}$) should simply be considered as sufficiently high for scoping purposes and should not be quantitatively compared.

In addition to differences in HT, differences between processing parameters also occurred. For the SR and SA HT conditions, the fracture toughness measured at an equivalent test temperature was lower for the

Tensile Blocks 02 build (VED ~52 J/mm^3) compared with the Tensile Blocks 01 build (VED ~71 J/mm^3). This difference is directly attributed to the porosity difference between the two builds, as previously shown in Figure 23. Although minor changes in grain orientation, morphology, and size existed between the two materials, the fracture toughness was identical as a function of temperature for the two builds after the same HIP treatment, where the grain structure was largely preserved and the porosity was closed in the Tensile Blocks 02 build. This result gives strong evidence that the root cause of the lower fracture toughness performance for the lower VED build was the lack-of-fusion porosity enabling easier crack propagation pathways through the LPBF 316H SS material.

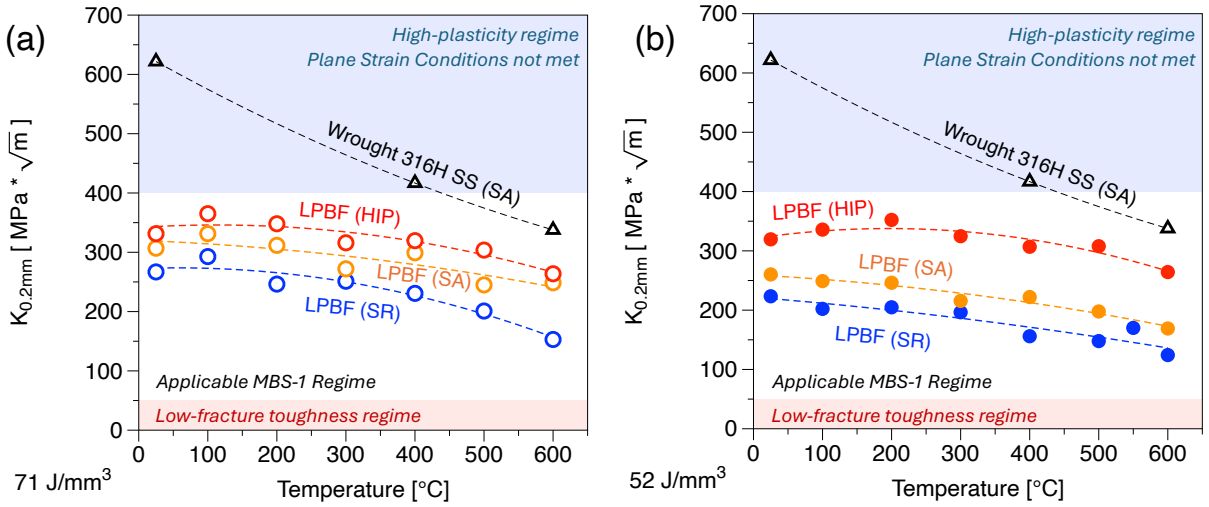

Figure 33. Fracture Toughness of LPBF 316H SS tested from 23°C to 600°C in comparison with reference tests on wrought 316H SS. Fracture toughness was compared for (a) Tensile Blocks 01 and (b) Tensile Blocks 02.

3.4 STRESS RELIEF OPTIMIZATION

At the start of the LPBF 316H SS qualification initiative, the initial heat treatments (Table 5) were chosen primarily by referencing prior optimization efforts for alloys such as additively manufactured 316L SS. More specifically, the SR HT was taken directly from prior work in the TCR program, where samples were subjected to this identical HT condition (650°C for 24 h) to ensure that thin tensile specimens extracted for neutron irradiations did not warp during machining because of residual stresses built up during printing [13].

One major difference separates the 316L SS investigated in TCR and the 316H SS investigated here—carbon content. The higher carbon content of 316H SS means that at temperatures >600°C [14], enhanced sensitization may begin to occur, which could decrease fracture toughness and promote corrosive attack in oxidative media. Therefore, it was important to evaluate both the extent of dislocation recovery and the extent of sensitization as a function of increasing HT temperature and time to develop a more appropriate SR HT for campaign testing.

Upon HT at 650°C, a carbide network began to form along the grain boundaries, as shown in Figure 34. Within just 15 min of heat exposure, carbide formation was evident, and the amount of carbide phase increased steadily with time, growing from 0.13 area % at 15 min to 2.5 area % after 6 h. To assess the effect of time and temperature on microstructural evolution concerning sensitization, a comparison across all temperatures for 15 min and 6 h samples is shown in Figure 34.

At 650°C [Figure 34(a) and (b)], the primary observation was an increase in carbide formation with time without any evidence of pitting. Additionally, the cell structure remained largely unchanged throughout the process. However, for the samples treated at 750°C, pitting along the grain boundaries became apparent after 6 h, accompanying the carbide networks that also formed along the boundaries [Figure 34(c) and (d)]. The cell structure also began to dissolve after 6 h at this temperature. For samples treated at 850°C, the cell structure rapidly dissolved, and pitting initiated within the first 15 min, becoming significantly more severe after 6 h [Figure 34(e) and (f)]. The overall size of the cellular structure, measured along the minor axis in the case of elongated cells, varied between 0.6 ± 0.07 and 1.0 ± 0.07 μm. This trend clearly shows that higher temperatures promote both carbide precipitation and sensitization, with pitting and structural degradation being much more pronounced at 850°C compared with the lower temperatures.

The average Vickers microhardness of the as-printed sample was 215 HV, as shown in Figure 35(a). After HT at 650°C, the hardness decreased to approximately 200 HV with little variation observed as the holding time increased, maintaining a consistent value around 200 HV. When the HT temperature was raised to 750°C and 850°C, the hardness further declined to around 190 HV and 180 HV, respectively. This result indicates a clear trend in which hardness decreased with increasing temperature, but the extended holding time at each respective temperature did not result in any significant further reduction in hardness. Similar trends were also seen when considering the dislocation density measured via XRD, which is shown in the same figure.

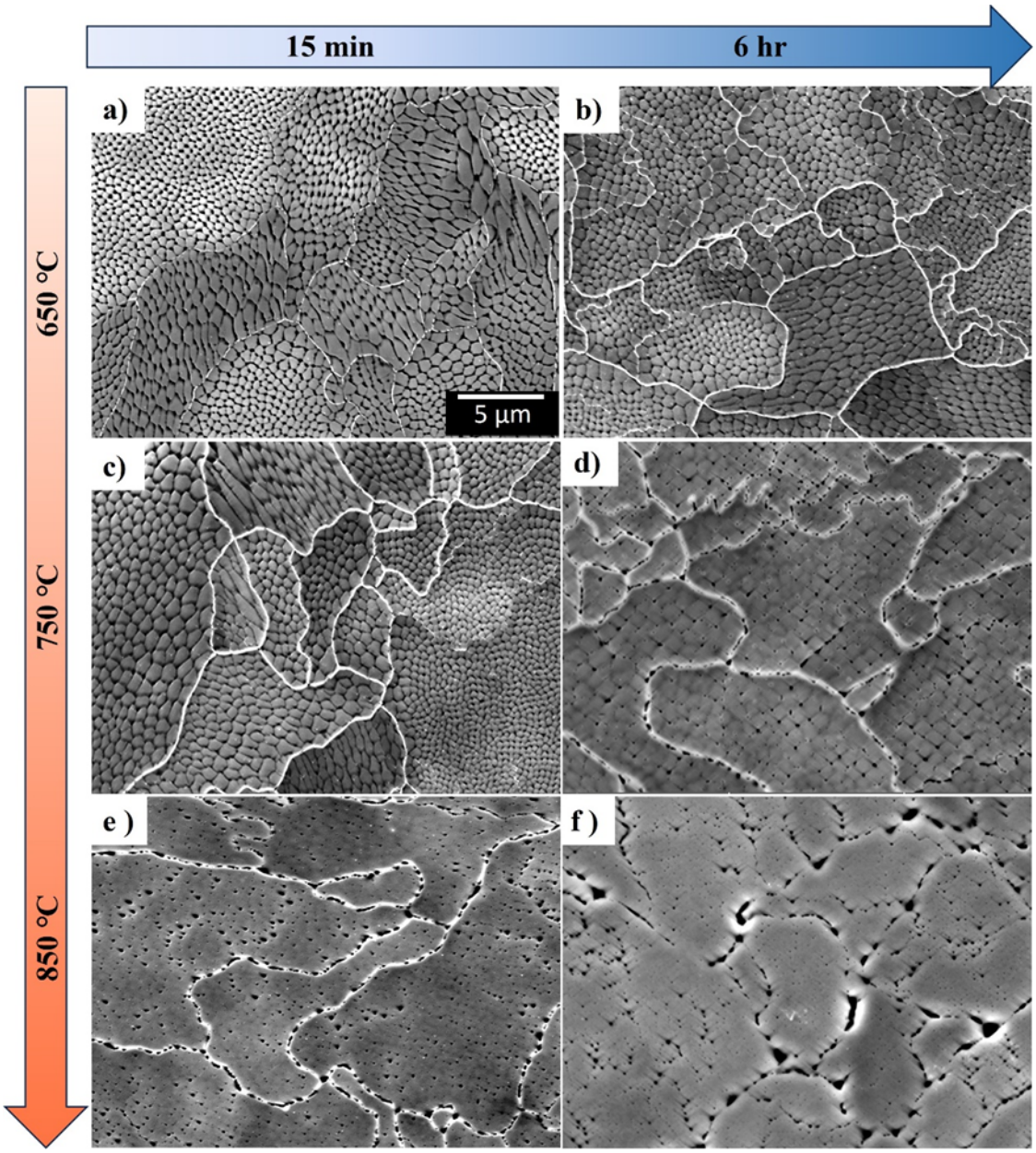

Figure 34: Secondary Electron SEM micrographs of electrolytically etched LPBF 316H SS samples following various SR HT at 650°C for (a) 15 min and (b) 6 h, 750°C for (c) 15 min and (d) 6 h, and 850°C for (e) 15 min

and (f) 6 h. All the micrographs are at the same magnification, and the micro marker is shown in Figure 4a.

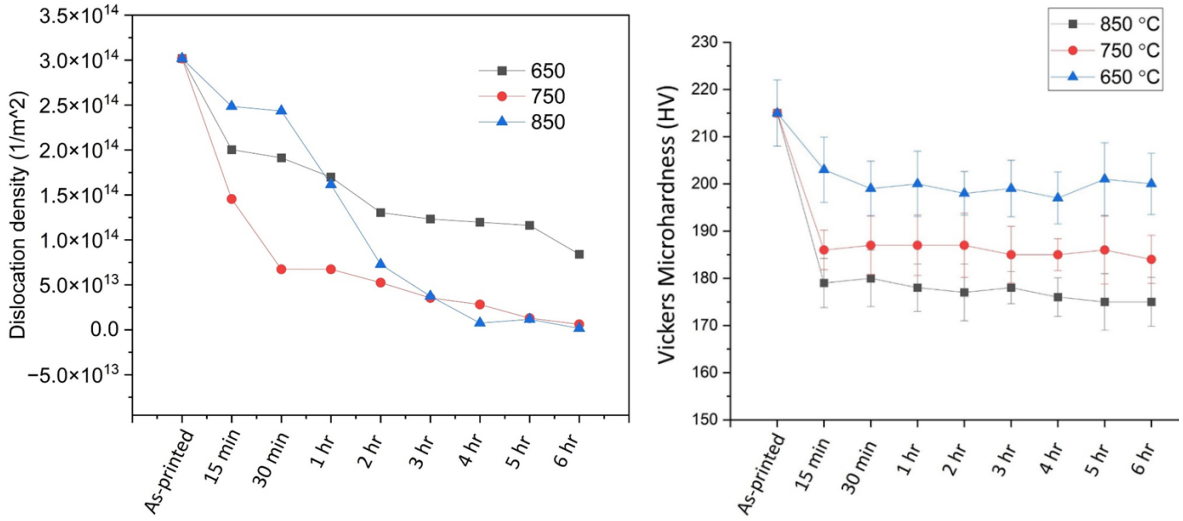

Figure 35. Evolution of (left) dislocation density calculated using modified Williamson–Hall analysis and (right) microhardness as a function of annealing temperature/time for cubes harvested from Tensile Blocks 02.

Based on this combination of SEM, XRD, and hardness investigations, LPBF 316H SS remains susceptible to sensitization even at 650°C, although the carbide coarsening kinetics remain relatively sluggish at this temperature. Similarly, the dislocation recovery kinetics also remain slow, and dislocation density decreases to only half the reduction that the 750°C and 850°C cases provide. Regardless, there does not appear to be an advantage of annealing components beyond 1–2 h, assuming that the LPBF components are relatively small in size and, thus, do not require significant hold times at temperature to alleviate temperature gradients in full-size, heat-treated components. This study recommends that for FY 2025, activities should include select stress-relieved specimens heat-treated at 650°C for 2 h rather than the 24 h employed in FY 2023 and FY 2024 creep and creep-fatigue tests.

4. CONCLUSIONS AND FUTURE WORK

This report summarizes work related to the fabrication and characterization of scaled builds for the AMMT campaign. In only 2 years, the process understanding work packages have (1) applied high-throughput characterization techniques to more rapidly down select printing conditions, leading to builds with minimized porosity; (2) scoped various post build heat treatments to identify differences in high-temperature performance; and (3) demonstrated scalability in printing with in situ process verification such that component-relevant sizes can be tested under neutron irradiation and for relevant code-case testing. As such, the process optimization work packages, including the work summarized here at ORNL, have been incredibly successful in rapidly increasing the readiness level of LPBF for 316H SS.

More importantly, this work has highlighted significant challenges that remain for the qualification of AM material—namely, the significant variations in material performance that exist with small changes in processing parameters, the question of anisotropy in LPBF components related to component-level design, and the differences in microstructures seen between prints performed at different locations using the same unit, parameters, and powder. These challenges are compounded with additional uncertainties related to wide variations in creep performance between builds, HTs, and processing conditions seen through testing at collaborating research institutions.

Future research is necessary to develop the integrated experiments and models necessary to identify the root causes of these sources of variability in LPBF 316H SS components. Only through this type of accelerated design-by-analysis approach will a rapidly expanding experimental matrix of specimens, both for code case and environmental effects testing, be effectively minimized. As such, future work will involve providing modeling teams the microstructural features extracted from the significant repository of specimens available for testing to compare with subsized and full-sized specimen performance data being generated across four different national laboratories for LPBF 316H SS going forward.

5. REFERENCES

[1] J. Clayton, D. Millington-Smith, B. Armstrong, "The Application of Powder Rheology in Additive Manufacturing", *Jom* 67(3) (2015) 544-548,
[2] Z. Wang, C. Jiang, P. Liu, W. Yang, Y. Zhao, M.F. Horstemeyer, L.-Q. Chen, Z. Hu, L. Chen, "Uncertainty Quantification and Reduction in Metal Additive Manufacturing", *Npj Computational Materials* 6(1) (2020) 175,
[3] P. Nandwana, A. Plotkowski, R. Kannan, S. Yoder, R. Dehoff, "Predicting Geometric Influences in Metal Additive Manufacturing", *Materials Today Communications* 25 (2020) 101174,
[4] I.F. Ituarte, E. Coatanea, M. Salmi, J. Tuomi, J. Partanen, "Additive Manufacturing in Production: A Study Case Applying Technical Requirements", *Physics Procedia* 78 (2015) 357-366,
[5] C. Massey, P. Nandwana, H. Hyer, S. Nayir, J. Kendall, C. Joslin, R. Duncan, D. Collins, T. Graening, F.L. III, L. Scime, Z. Snow, A. Ziabari, T. Butcher, R. Dehoff, "Data-Driven Optimization of the Processing Window for 316h Components Fabricated Using Laser Powder Bed Fusion", Oak Ridge National Laboratory(2023),
[6] A. Committee, A. ASTM, "240/a 240m-04a: Standard Specification for Chromium and Chromium-Nickel Stainless Steel Plate, Sheet, and Strip for Pressure Vessels and for General Applications", *ASTM International* (2004),
[7] Y.C. Xuan Zhang, Srinivas Aditya Mantri, Lin Gao, Edward Listwan, Joe Listwan, Michael McMurtrey, Ninad Mohale, Caleb Massey, "Fy24 Integrated Results for High-Temperature Mechanical Testing of Lpbf 316h Stainless Steel. ", Argonne National Laboratory,
[8] T. Byun, S. Maloy, J. Yoon, "Small Specimen Reuse Technique to Evaluate Fracture Toughness of High Dose Ht9 Steel", Sixth International Symposium on Small Specimen Test Techniques, ASTM International, (2014), 1-22,
[9] M.A. Chaudry, G. Mohr, K. Hilgenberg, "Experimental and Numerical Comparison of Heat Accumulation During Laser Powder Bed Fusion of 316l Stainless Steel", *Progress in Additive Manufacturing* 7(5) (2022) 1071-1083,
[10] G. Mohr, S.J. Altenburg, K. Hilgenberg, "Effects of Inter Layer Time and Build Height on Resulting Properties of 316l Stainless Steel Processed by Laser Powder Bed Fusion", *Additive Manufacturing* 32 (2020) 101080,
[11] A. Chniouel, P.-F. Giroux, F. Lomello, P. Aubry, É. Vasquez, O. Hercher, H. Maskrot, "Influence of Substrate Temperature on Microstructural and Mechanical Properties of 316l Stainless Steel Consolidated by Laser Powder Bed Fusion", *The International Journal of Advanced Manufacturing Technology* 111 (2020) 3489-3503,
[12] L. Chechik, N.A. Boone, L.R. Stanger, P. Honniball, F. Freeman, G. Baxter, J.R. Willmott, I. Todd, "Variation of Texture Anisotropy and Hardness with Build Parameters and Wall Height in Directed-Energy-Deposited 316l Steel", *Additive Manufacturing* 38 (2021) 101806,
[13] L. Scime, M. Sprayberry, D. Collins, A. Singh, C. Joslin, R. Duncan, J. Simpson, F. List III, K. Carver, A. Huning, J. Haley, V. Paquit, "Diagnostic and Predictive Capabilities of the Tcr Digital Platform", United States, (2021), 10.2172/1831630
[14] D. Peckner, I.M. Bernstein, "Handbook of Stainless Steels", McGraw-Hill Book Co., New York, (1977),